25th Anniversary Article: Understanding the Lithiation of Silicon and Other Alloying Anodes for Lithium-Ion Batteries

*Matthew T. McDowell, Seok Woo Lee, William D. Nix, and Yi Cui**

Alloying anodes such as silicon are promising electrode materials for next-generation high energy density lithium-ion batteries because of their ability to reversibly incorporate a high concentration of Li atoms. However, alloying anodes usually exhibit a short cycle life due to the extreme volumetric and structural changes that occur during lithium insertion/extraction; these transformations cause mechanical fracture and exacerbate side reactions. To solve these problems, there has recently been significant attention devoted to creating silicon nanostructures that can accommodate the lithiation-induced strain and thus exhibit high Coulombic efficiency and long cycle life. In parallel, many experiments and simulations have been conducted in an effort to understand the details of volumetric expansion, fracture, mechanical stress evolution, and structural changes in silicon nanostructures. The fundamental materials knowledge gained from these studies has provided guidance for designing optimized Si electrode structures and has also shed light on the factors that control large-volume change solid-state reactions. In this paper, we review various fundamental studies that have been conducted to understand structural and volumetric changes, stress evolution, mechanical properties, and fracture behavior of nanostructured Si anodes for lithium-ion batteries and compare the reaction process of Si to other novel anode materials.

1. Introduction

The Li-ion battery has become the energy storage device of choice for portable electronic devices such as smart phones, laptop computers, and tablet PCs due to its high energy density.[1–3] However, emerging electric transportation systems, including hybrid electric vehicles (HEVs), plug-in hybrid electric vehicles (PHEVs), and fully electric vehicles (EVs) require batteries with even higher specific energy, energy density, and cycle life, along with lower cost and improved safety. Most mass-producible EVs are limited to a relatively short traveling distance per charge (~160 km) due to limitations of specific energy/energy density and also the cost of the battery system. To address this issue, the United States Advanced Battery Consortium (USABC) has put in place long-term goals for electric vehicle batteries to guide research in this area.[4] The energy density and specific energy requirements put forth for battery pack systems are 300 Wh L^{-1} and 200 Wh kg^{-1} at a C/3 discharge rate (a C/3 rate corresponds to complete discharge in three hours), and the battery is required to cycle 1000 times with a maximum of 20% capacity degradation. One way to achieve these goals is to pursue the development of new electrode materials with higher specific capacity than traditional materials, while maintaining the required cycle life. High capacity materials can increase energy content per weight and volume while reducing the cost per energy unit, although they also present new materials challenges.

In commercial Li-ion batteries, the usual positive electrode materials are metal oxides or phosphates (such as $LiCoO_2$, $LiMnO_2$, or $LiFePO_4$), and the negative electrode is graphite. Both the positive and negative electrode materials react with Li via an intercalation mechanism: Li ions or atoms reside in interstitial sites within the host lattice, and the insertion/extraction of Li results in only small strains and minimal irreversible structural changes in the host material. As a result, the intercalation mechanism can result in good capacity retention over many cycles, but the specific capacity of these materials is relatively low due to the limited number of intercalation sites for Li ions within the host lattice. In contrast, negative electrode materials such as Si, Ge, and Sn react with Li via a different mechanism: Li forms alloys with these materials, which involves breaking the bonds between host atoms, causing dramatic structural changes in the process.[5–9] Since the atomic framework of the host does not constrain the reaction, anode materials that form alloys can have much higher specific capacity than intercalation electrode materials. For instance, the equilibrium Li-Si alloy with the highest Li concentration is the $Li_{22}Si_5$ phase, which is much more Li-rich than fully-lithiated graphite (LiC_6).[6] In terms of theoretical specific capacity, the Li-Si alloy phase can attain 4200 mAh g^{-1} while graphite exhibits only 372 mAh g^{-1}. The theoretical specific capacities for other alloying anodes,

Dr. M. T. McDowell,[+] Dr. S. W. Lee,[+] Prof. W. D. Nix, Prof. Y. Cui
Department of Materials Science and Engineering
Stanford University
Stanford, CA 94305, USA
E-mail: yicui@stanford.edu
Prof. Y. Cui
Stanford Institute for Materials and Energy Sciences, SLAC National Accelerator Laboratory
2575 Sand Hill Road, Menlo Park, CA 94025, USA
[+]These authors contributed equally.

DOI: 10.1002/adma.201301795

such as Ge and Sn, are also very high (1623 and 994 mAh g^{-1}, respectively). However, the large number of Li atoms that can be inserted into these materials causes extreme volume changes (310% for full lithiation of Si).[10] The volumetric and structural changes during Li insertion and extraction usually result in rapid decay of the specific capacity with cycling due to mechanical fracture/decrepitation of particles and irreversible side reactions with the organic electrolyte that are exacerbated by volume changes.[6,11–13] One mechanism by which fracture is thought to cause capacity decay is via the electrical isolation of fractured active material fragments. Preventing mechanical fracture and diminishing the significance of side reactions in these anode materials during electrochemical Li insertion and extraction is therefore essential for utilizing their high specific capacity for long-lasting, higher energy density Li-ion batteries.

Among the many candidate alloying anode materials, Si is considered one of the most promising because of its exceptionally high specific capacity, its abundance in the earth's crust, and the benefits of a well-developed industrial infrastructure for manufacturing. Si has been studied for use in Li batteries for more than three decades,[14,15] but mechanical degradation and capacity decay have typically prevented good cycling performance. In early 2008, our group demonstrated that Si nanowire anodes can be used to mitigate mechanical fracture, opening up the opportunity to use nanomaterials design to address these issues.[12] Since then, various Si nanostructures have shown promise for improved cycle life.[12,16–27] Nanostructured Si anodes are advantageous for a number of reasons, including for their ability to accommodate lithiation-induced strain without fracture and their good rate capability.[28,29] Si nanostructures such as nanowires, nanoparticles, and nanotubes have been designed and fabricated for use in Li-ion batteries.[12,17,26,30] In addition, some nanostructures have been specifically engineered with volume change as a key design factor, including core-shell nanotubes and yolk-shell type nanoparticle assemblies.[18,22,23] The surface chemistry and structure of nanostructured electrodes have also been studied.[31–33] The success of these designs, as summarized in one of our recent reviews,[34] illustrates the importance of understanding and controlling the effects of volume change in nanostructured Si anodes. In general, it is vital to develop a fundamental understanding of how the size, shape, and crystallinity of Si nanostructures affect volume expansion, stresses, and fracture; this knowledge can in turn be used to design structures with improved electrochemical performance and can also guide the development of other alloying anode materials.[35] Furthermore, from a scientific perspective, the influence of stress and volume change on the thermodynamics and kinetics of this solid-state transformation is of particular interest. With this motivation, there has been much attention focused on understanding the volume changes, stress evolution, and mechanical failure during the lithiation/delithiation of Si. In this review, we discuss the fundamental aspects of the Li-Si electrochemical reaction and also the factors that influence fracture in Si anodes.

This review is organized in the following manner. First, the physical processes, structural changes, and volume expansion/contraction during the lithiation/delithiation of Si will be discussed. Next, the effect of Si crystallography on volume expansion will be examined. Modeling efforts to understand

Matthew McDowell received his B.S. in materials science and engineering from Georgia Tech in 2008, and he recently finished his Ph.D. in Prof. Yi Cui's lab at Stanford University. His current research involves studying electrochemical transformations in high capacity battery electrode materials, and he is broadly interested both in electrochemical systems and the dynamic properties of nanomaterials and interfaces.

Seok Woo Lee received his B.S. in mechanical engineering from Pohang University of Science and Technology (POSTECH) in 2003 and his Ph.D. in mechanical engineering from Korea Advanced Institute of Science and Technology (KAIST) in 2008. Currently, he is a research associate in the Geballe Laboratory for Advanced Materials at Stanford University. His research interests are in electrochemical systems for energy storage and harvesting.

William D. Nix received his Ph.D. from Stanford University in 1963. Since then, he has been involved in studying the mechanical properties of a wide variety of materials. In recent years, his research has focused on nanoscale size effects on mechanical properties and also the mechanics of high-capacity lithium battery electrodes. He is a member of the National Academy of Engineering and the National Academy of Sciences.

Yi Cui received his B.S. in chemistry from the University of Science and Technology of China in 1998 and his Ph.D. from Harvard University in 2002, followed by work as a Miller Postdoctoral Fellow at the University of California, Berkeley. In 2005, he became a professor in the Department of Materials Science and Engineering at Stanford University. He leads a group of researchers working on nanomaterials for energy, electronics and biotechnology.

DOI: 10.1002/adma.201301795

mechanical stress evolution and fracture, along with related experiments, will then be presented. Finally, the review will conclude with a section comparing the Li-Si alloying reaction to reaction processes in other novel anode materials.

2. Electrochemical Lithiation of Crystalline Si

Many Si electrodes that have been developed and tested utilize crystalline Si as the active material. It has been commonly demonstrated that the first lithiation of crystalline Si results in significant irreversible capacity loss[12,36] and substantial particle fracture.[37] To understand these processes, it is necessary to study the structural changes and volume expansion during lithiation of crystalline Si structures. In the following section, studies on the lithiation and amorphization of crystalline Si will be presented, and aspects related to electrochemical behavior, crystallization of lithiated Si, and material properties will be discussed.

2.1. Two-Phase Lithiation and Electrochemical Solid-State Amorphization

Crystalline Si is electrochemically lithiated via a two-phase mechanism in which the Si is consumed to form lithiated amorphous Si (Li_xSi), and the two phases are separated by a sharp reaction front of nanometer scale thickness.[9,38–41] On a fundamental level, this two-phase behavior likely occurs because of the large activation energy required to break up the crystalline Si matrix: a high concentration of Li atoms near the reaction front is required to weaken the Si-Si bonds, leading to favorable lithiation kinetics and the observed two-phase behavior.[39,41] The lithiated amorphous phase that forms at the expense of the crystalline Si is highly lithiated, with $x = 3.4 \pm 0.2$ Li atoms per Si atom (this is close to the stoichiometry of the commonly reported terminal crystalline phase at room temperature, where $x = 3.75$).[42] The formation of highly lithiated Si at the reaction front causes most of the volume expansion to occur right at the front, which leads to enormous gradients in transformation strain.

A few early studies focused on this unique electrochemical solid-state amorphization process.[9,40] In the Li-Si system, four intermediate equilibrium phases have been found to form during equilibrium Coulometric titration experiments of Li in Si electrodes at high temperature (415 °C).[14] The nominal compositions of these phases are $Li_{12}Si_7$, Li_7Si_3, $Li_{13}Si_4$, and $Li_{22}Si_5$. The sequential formation of these compounds results in a stepped galvanostatic voltage profile during high-temperature electrochemical experiments, as shown in **Figure 1**. At room temperature, however, the galvanostatic voltage profile of typical crystalline Si electrodes during lithiation shows a relatively flat voltage plateau around 0.1 V that suggests a two-phase field over most of the lithiation process; this is demonstrated by the example voltage curve for a half cell with a Si powder working electrode (Figure 1).[9] Ryu et al. showed similar behavior using the more precise galvanostatic intermittent titration technique (GITT) for a crystalline Si particle electrode upon lithiation.[43] The single voltage plateau observed during room-temperature alloying of Li with crystalline Si (solid line in Figure 1) is clearly different than the equilibrium voltage profile at high temperature (dotted line in Figure 1).[14] This is because the room temperature lithiation process involves electrochemical solid-state amorphization and results in the formation of a metastable amorphous Li_xSi phase instead of the equilibrium intermetallic compounds. Solid-state amorphization occurs because the formation of the equilibrium phases is kinetically hindered, so the amorphous phase (which has lower Gibbs free energy than the reactants) forms.[9] Experimentally, the amorphization process was explored by Limthongkul et al. with X-ray diffraction and high-resolution electron microscopy experiments.[9] More recently, the two-phase structure of the amorphous Li_xSi/crystalline Si interface was imaged with scanning electron microscopy (SEM) and high-resolution transmission electron microscopy (HRTEM).[38,41]

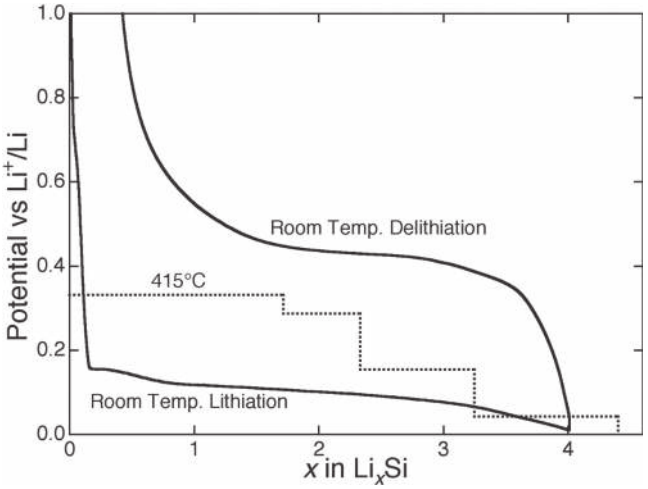

Figure 1. Coulometric titration curve for the Li-Si system at 415 °C (dotted line) and galvanostatic charge/discharge of a Si powder electrode at room temperature (solid line). The stepped voltage profile of the high temperature experiment is indicative of a series of two-phase reactions. In contrast, room-temperature lithiation shows a single gradually sloping plateau and large hysteresis between lithiation and delithiation. The high temperature data is taken from ref. [14].

2.2. Crystallization of Highly Lithiated Amorphous Si

According to the equilibrium Coulometric titration at high temperature (415 °C) and the phase diagram, $Li_{22}Si_5$ is the most Li-rich phase of the Li-Si system, and the theoretical maximum specific capacity upon lithiation of Si is commonly calculated as 4200 mAh g^{-1} by considering this phase.[14,44,45] However, several studies have shown that the final phase of lithiated Si at room temperature is not $Li_{22}Si_5$. Obrovac et al. studied structural changes during the Li-Si alloying process using ex situ X-ray powder diffraction.[8] They found that when the potential of the electrode falls below about 50 mV vs Li/Li^+, highly lithiated amorphous Si suddenly crystallizes to form the $Li_{15}Si_4$ phase instead of $Li_{22}Si_5$. The $Li_{15}Si_4$ phase is not an equilibrium phase but is instead metastable. Chevrier and Dahn have noted that the $Li_{15}Si_4$ phase is the only crystalline Li-Si phase in which all the Si atoms have equivalent crystallographic sites; each Si atom has 12 Li neighbors.[46] First principles simulations and experiments have shown that in the amorphous phase before

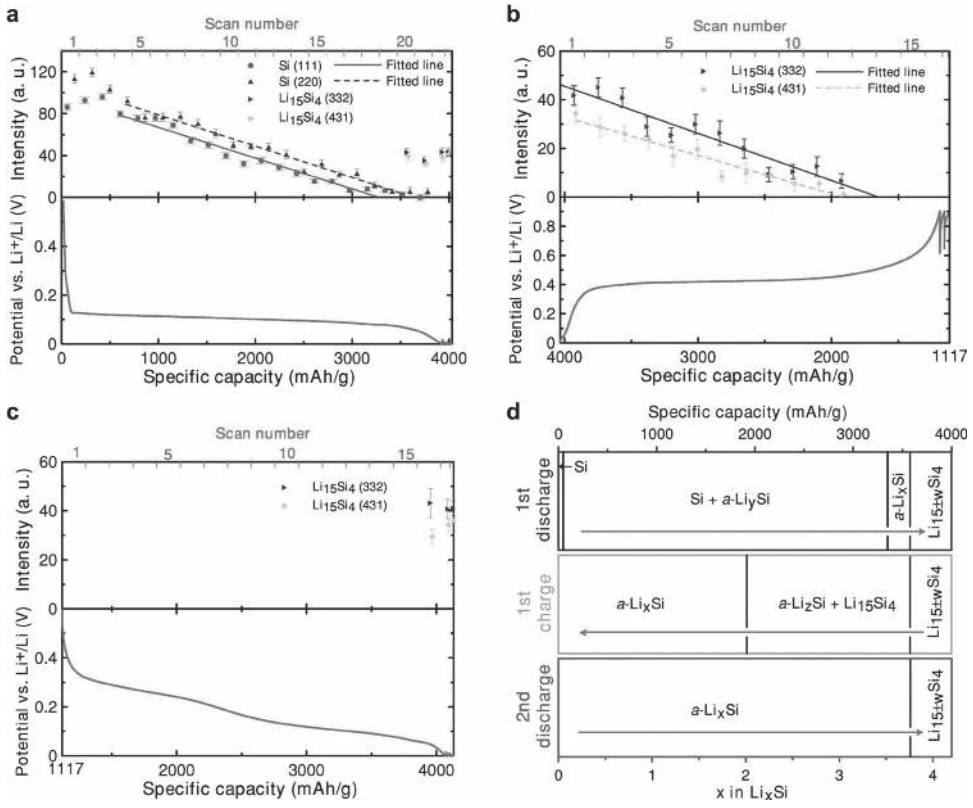

Figure 2. In situ X-ray diffraction during galvanostatic cycling of a crystalline Si electrode in a half cell at room temperature. In panels (a-c) the potential profiles are shown in the bottom sections, and corresponding plots of the intensities of different Bragg peaks during cycling of the cell are shown in the top sections. The cycling rate was C/100. a) Potential profile and the intensity of two Si peaks and two $Li_{15}Si_4$ peaks during the first discharge (lithiation) of the crystalline Si. As the crystalline Si is lithiated, the Si peaks gradually disappear as amorphous Li_ySi (a phase with fixed composition) forms via a two-phase reaction. The amorphous lithiated phase crystallizes into the $Li_{15}Si_4$ phase when the potential decreases below ~60 mV. b) Potential profile and the intensity of two $Li_{15}Si_4$ peaks during the first charge (delithiation). The $Li_{15}Si_4$ peaks disappear as the material is delithiated, eventually forming amorphous Si at the end of charge. c, Potential profile and the intensity of two $Li_{15}Si_4$ peaks during the second discharge. The lithiated material remains amorphous until the end of discharge, when the $Li_{15}Si_4$ phase reappears. d) Schematic summarizing the phases that form as a function of specific capacity during the charge–discharge cycling of a Li/Si electrochemical cell at room temperature. The $Li_{15\pm w}Si_4$ notation designates that this phase has slightly variable stoichiometry. The Li_ySi, Li_xSi, and Li_zSi notation represent amorphous Li-Si phases with different compositions; Li_ySi and Li_zSi are amorphous phases with a fixed composition, while the Li content in Li_xSi varies. Reproduced with permission.[47] Copyright 2007, The Electrochemical Society.

$Li_{15}Si_4$ crystallization, Si atoms are well dispersed and mostly surrounded by Li atoms.[42,46] This suggests that the similarities in the local atomic environments in the lithiated amorphous phase and the crystalline $Li_{15}Si_4$ phase might lead to kinetically-favored crystallization of the metastable phase instead of the formation of a thermodynamically stable phase. Upon delithiation of the crystalline $Li_{15}Si_4$ phase, the material transforms back to amorphous Si. An in situ X-ray diffraction study performed by Li et al. also confirmed these results;[47] **Figure 2**a-c show the intensity of the Bragg peaks of the Si and $Li_{15}Si_4$ phases along with the corresponding electrochemical potential profile during the first lithiation, the first delithiation, and the second lithiation. During the first lithiation (Figure 2a), the crystalline Si peaks decrease in intensity with increasing capacity due to the disappearance of Si and the formation of amorphous Li_xSi. At the end of the first lithiation (when the potential drops below about 60 mV vs Li/Li^+), $Li_{15}Si_4$ peaks appear as the highly lithiated amorphous Li_xSi phase crystallizes into $Li_{15}Si_4$. During the first delithiation (Figure 2b), the intensity of the $Li_{15}Si_4$ peaks decreases linearly with time, but crystalline Si peaks are not detected again because the Si at the end of charge remains amorphous throughout cycling. During the second lithiation (Figure 2c), the amorphous Li_xSi phase again crystallizes into the $Li_{15}Si_4$ phase when the electrode potential decreases below about 60 mV. Figure 2d shows a summary of the phase transformations that occur during cycling. The sudden crystallization of the $Li_{15}Si_4$ phase during room temperature lithiation has also been observed with electron diffraction during the lithiation of Si nanowires and nanoparticles with in situ TEM.[29,48–51] Overall, the vast majority of studies have reported the formation of $Li_{15}Si_4$ as the terminal phase, which supports the belief that $Li_{15}Si_4$ is the most highly lithiated phase at room temperature. It should be noted that a few TEM studies have reported the existence of the $Li_{22}Si_5$ phase; however, this might be a result of the specific conditions used in these works.[52,53]

Further work has been devoted to clarifying how the temperature during lithiation affects the terminal crystalline phase formed. Using X-ray diffraction, Kwon et al. showed the emergence of the $Li_{21}Si_5$ phase at higher temperatures during lithiation of a Si thin film.[54] It should be noted that there has

DOI: 10.1002/adma.201301795

been debate in the literature about the differences between the $Li_{22}Si_5$ and the $Li_{21}Si_5$ phases; in most cases, the two phases are not differentiated.[55] This study found that the $Li_{15}Si_4$ phase is formed as the terminal phase below about 85 °C, but the $Li_{21}Si_5$ phase forms at the end of lithiation at temperatures higher than 100 °C. It was also found that if Si is lithiated at room temperature but the voltage is held at 0 V vs Li/Li^+ after lithiation, the $Li_{21}Si_5$ Bragg peaks begin to develop after about 24 hours.[54] This suggests that the metastable $Li_{15}Si_4$ phase can transform to the thermodynamically stable phase if given sufficient time. In another informative study, Key et al. performed in situ and ex situ nuclear magnetic resonance (NMR) to shed light on some of the properties of the metastable $Li_{15}Si_4$ phase.[42] This phase was shown to accommodate some nonstoichiometry (i.e., it is not a line compound), and it was also observed to undergo a self-discharge mechanism in which Li from this phase reacts with the electrolyte and is lost from the electrode when the cell is held at the open circuit potential. This important observation is potentially a source of capacity loss in batteries with Si anodes, and further study on how to mitigate this effect is warranted. We note that the formation of the lithiated crystalline phase might depend on a number of variables, including temperature, lithiation rate, the size of the starting Si material, and whether the Si is crystalline or amorphous.

In summary, the lithiation of crystalline Si occurs via a two-phase reaction in which highly lithiated amorphous Si forms at room temperature instead of equilibrium phases. In addition, the metastable $Li_{15}Si_4$ phase is commonly found to form when the voltage decreases below about 50 mV during lithiation.

3. Anisotropic Lithiation and Volume Expansion of Crystalline Si

As mentioned previously, fracture due to large volume changes during lithiation and delithiation is a significant cause of capacity decay in Si anodes. To understand fracture, it is first necessary to understand the nature of expansion and contraction during lithiation/delithiation and to relate this to stress evolution in different Si structures. Acoustic emission studies during the electrochemical cycling of initially crystalline Si particles have shown that more fracture events take place during the initial crystalline-to-amorphous transformation than during subsequent cycling.[37] This indicates that it is also essential to understand the differences in volume expansion in amorphous and crystalline Si. In this section, experimental observations of the volume expansion behavior of crystalline Si are discussed.

To study the effect of crystallography on lithiation and volume expansion, well-defined single crystalline Si structures are necessary. Studies of this type have utilized Si micro/nanostructures either etched from single crystalline Si wafers or fabricated through bottom-up techniques (such as Si nanowires). Using ex situ or in situ electron microscopy, volume changes during or after lithiation/delithiation have been monitored in individual structures. There have been a few independent studies that established the existence of anisotropic lithiation in crystalline Si; these works are detailed below.

In one study, Lee et al. examined the lithiation-induced shape and volume changes of crystalline Si nanopillars with different crystallographic orientations.[56] Si nanopillars with three

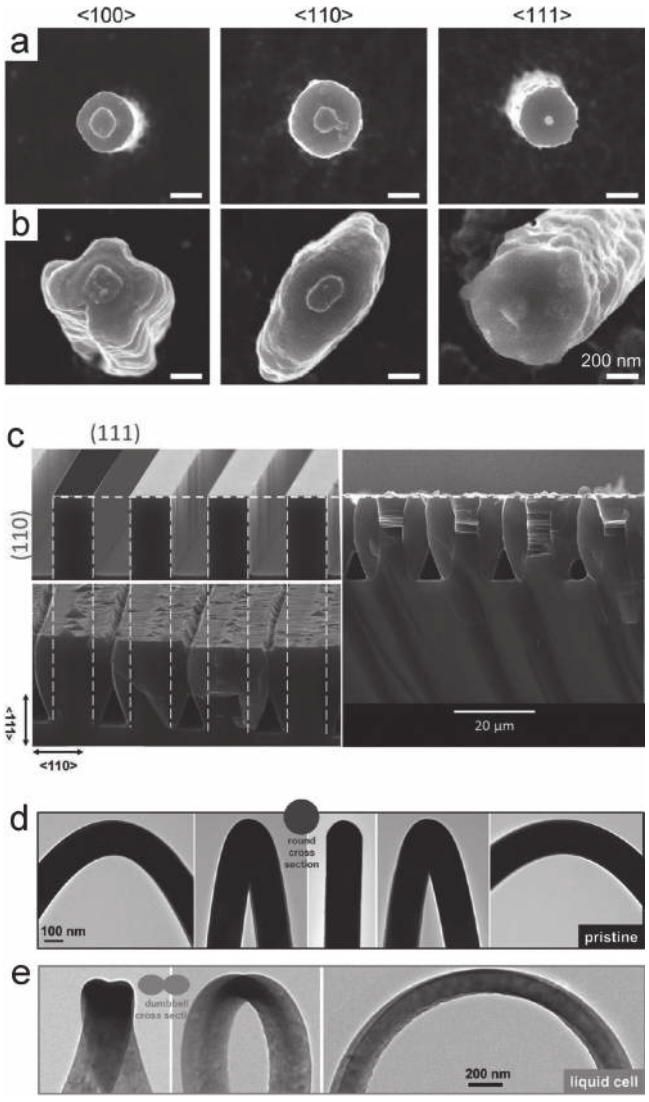

Figure 3. Experiments revealing anisotropic lithiation and expansion of crystalline Si nanostructures. a,b) SEM images demonstrating anisotropic lateral expansion upon lithiation of crystalline Si nanopillars with three different axial orientations (<100>, <110>, and <111>). The top row (a) shows pristine pillars, and the second row (b) shows fully lithiated pillars. After lithiation, volume expansion is observed to occur along <110> directions perpendicular to the nanopillar axis. Reproduced with permission.[56] Copyright 2011, American Chemical Society. c) Cross-sectional SEM image of a patterned (111) single-crystalline Si wafer with {110} (sidewalls) and {111} (top surface) crystal planes exposed to the electrolyte before (left) and after (right) galvanostatic lithiation. After lithiation, the Si was observed to primarily expand laterally in the <110> directions, with only negligible expansion in the [111] direction. Reproduced with permission.[57] Copyright 2011, WILEY-VCH Verlag GmbH & Co. d,e) In situ TEM images of anisotropic swelling of a Si nanowire during lithiation. The pristine nanowire (d) has two lateral {110} surfaces and a round cross section. After lithiation, the nanowire expands into a dumbbell shape, with preferential expansion occurring at the lateral {110} surfaces. Reproduced with permission.[58] Copyright 2011, American Chemical Society.

different axial orientations (<100>, <110>, and <111>) were fabricated on Si wafers (**Figure 3**a). These wafers were then used as the working electrodes in conventional electrochemical half-cells. After potentiostatic lithiation, it was found that the

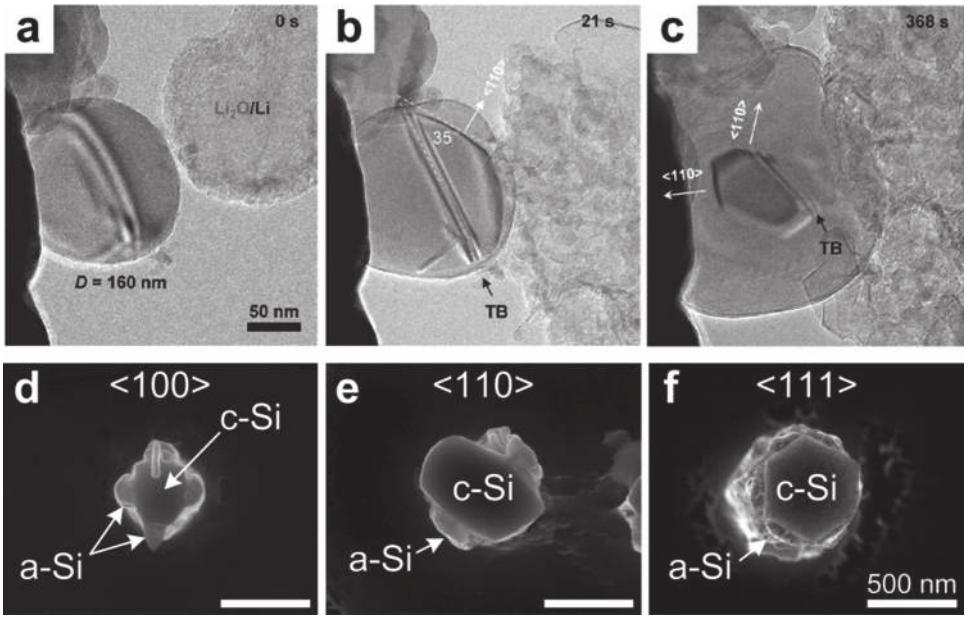

Figure 4. a-c) In situ TEM images of the electrochemical lithiation of a Si nanoparticle with an initial diameter of about 160 nm. a) Pristine nanoparticle. b) The same particle after 21 s of lithiation. Fast swelling at the labeled (110) surface is visible, and the (110) plane is flattened. There is a twin boundary in the particle (labeled TB). c) With further lithiation, the crystalline core becomes highly faceted, with flat {110} planes visible at the crystalline core. Reproduced with permission.[29] Copyright 2012, American Chemical Society. d-f) SEM images of Si nanopillars with three different axial orientations (<100>, <110>, and <111>) after partial lithiation and subsequent removal of the lithiated phase to expose the crystalline cores. The cores of the pillars display flattened {110} surfaces at the sidewalls. Both of these experiments show that during lithiation, the shrinking crystalline Si cores are bound by flat {110} planes. Reproduced with permission.[59] Copyright 2012, WILEY-VCH Verlag GmbH & Co.

initially circular cross sections of nanopillars with <100>, <110>, and <111> axial orientations expanded into cross, ellipse, and hexagonal shapes, respectively, as shown in Figure 3b. These shapes form because most volume expansion occurs at the {110} surfaces on the sidewalls of the pillars. For example, pillars with a <110> axial orientation have two {110} side surfaces and two {100} side surfaces, leading to preferential expansion along two radial directions. Dimensional expansion ratios along lateral <110> and <100> directions were measured to be 245% and 49%, respectively, which means that in this case, the {110} surfaces experience approximately five times greater dimensional change than the {100} surfaces. The average overall volume expansion ratios of pillars with <100>, <110>, and <111> axial orientations were measured to be 242.7%, 270.8%, and 263.8%, respectively.

In another study, Goldman et al. fabricated arrays of Si bar structures by photolithography and deep reactive ion etching (RIE), and volume expansion after lithiation was observed using ex situ SEM, as shown in Figure 3c.[57] On a (111) wafer, the pristine bar structures have {110} planes on the sidewalls and {111} planes on the top surfaces of the bars. Galvanostatic lithiation caused volumetric expansion to predominantly occur at the lateral {110} sidewalls, and expansion at the (111) top surface was negligible (Figure 3c). When similar bar structures were patterned on a (110)-oriented wafer, {111} planes were exposed at the sidewalls. These structures showed volumetric expansion primarily at the (110) top surface planes, resulting in vertical extension of the bars after galvanostatic lithiation.

In a third related study, Liu et al. reported the direct observation of the anisotropic swelling of Si nanowires during lithiation using in situ TEM.[58] The Si nanowires had <112> axial orientations; thus, there are two {110} surfaces at the sidewalls with normals that are 180° from each other. Figure 3d shows TEM images of the round cross-sectional shape of a pristine Si nanowire of this type. Upon lithiation, it was found that the volumetric expansion of the Si nanowire is highly anisotropic, resulting in a dumbbell-shaped cross section as shown in Figure 3e. The greater volume expansion occurred at the {110} sidewalls, and the dimensional expansion ratio along the <110> lateral direction was roughly eight times greater than that along the <111> direction.

To determine the underlying causes of anisotropic expansion, it is helpful to examine the structure of the reaction front. To this end, Liu et al. studied the lithiation of individual crystalline Si nanoparticles in real time with in situ TEM.[29] **Figure 4**a-c show TEM images during lithiation of a Si nanoparticle containing a twin boundary in the center of the particle. The particle shows bumps at the outer surface due to preferential expansion at {110} surfaces. Underneath these bumps, flat {110} facets are found at the boundary of the crystalline core. As the crystalline core of the particle shrinks during lithiation, the flat {110} facets propagate inward and disappear after the particle is fully lithiated. In a similar study, Lee et al. studied the shape of the crystalline Si core in partially lithiated Si nanopillars with <100>, <110>, and <111> axial orientations.[59] The nanopillar electrodes were partially lithiated in conventional

Adv. Mater. **2013**,
DOI: 10.1002/adma.201301795

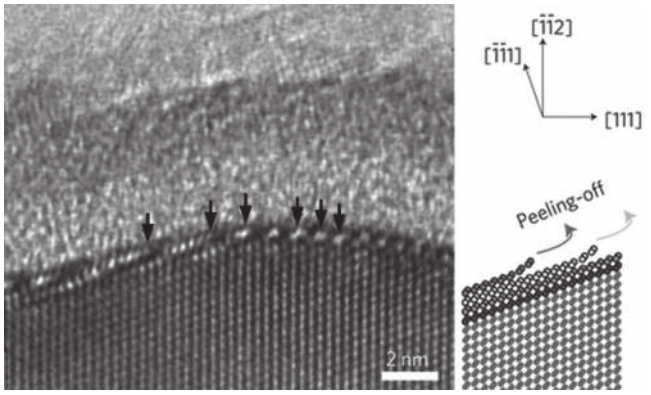

Figure 5. High-resolution in situ TEM image of a {112}-oriented Si/Li_xSi reaction front during the lithiation of a crystalline Si nanowire. The amorphous/crystalline interface region is a few atoms thick, and the crystalline Si lattice is highly distorted in this region. {111} Si planes at the reaction front are marked by arrows. As shown in the accompanying schematic, the Si lattice is broken up by Li penetration between {111} planes at the interface and the peeling off of these planes. Thus, the orientation of {111} planes with respect to the interface controls the reaction rate at the interface and leads to anisotropic expansion during lithiation. Reproduced with permission.[41] Copyright 2012, Macmillan Publishers Ltd.

electrochemical cells, and then they were removed from the cells and the Li_xSi shell was etched away with methanol.[60] Subsequent SEM observation revealed the shape of the crystalline cores (Figure 4d-f). For each of the three axial orientations (Figure 4d-f), the crystalline Si core is bound by relatively flat {110} surfaces. Although these studies do not reveal atomic-scale mechanisms, they suggest that anisotropic expansion is due to differences in interfacial mobility of different crystallographic planes: the flat {110} planes are observed because they react the fastest.

Recently, in situ TEM experiments by Liu et al. have revealed the atomic-scale mechanisms of the lithiation process and have verified that anisotropic expansion is due to differences in interfacial mobility of different crystallographic planes during lithiation.[41] It was found that it is kinetically easier for Li atoms to penetrate and break up the crystalline Si lattice along <110> and <112> lateral directions than along <111> directions. Interestingly, a ledge mechanism of lithiation was directly observed, in which layer-by-layer peeling of {111} facets controls the kinetics of the lithiation process, as shown in **Figure 5**. Li penetration through close-packed {111} planes was never observed; instead, these planes were peeled off and broken up into individual Si atoms.[41]

Taken together, these experiments have established that anisotropic lithiation and expansion is primarily a result of differing interfacial mobilities of different crystallographic planes. Diffusion of Li in crystalline Si does not play a role since the symmetry elements of a cubic crystal mathematically result in isotropic diffusivity.[61] Assuming fast enough Li diffusion through the amorphous Li_xSi phase to reach the crystalline core in a nanostructure, this type of reaction process would result in reaction front-limited kinetics for lithiation of crystalline Si nanostructures.[62,63] These conclusions have also been supported by direct electrochemical measurements[64] and by finite element modeling efforts. By assigning different reaction front velocities to different crystallographic surfaces in finite element simulations of volume expansion and plastic deformation during the lithiation of Si, a few studies have reproduced the experimentally observed lithiated nanopillar cross sections.[62–64] This supports the theory that anisotropic expansion during the lithiation of crystalline Si is a result of the interface-limited reaction with differing reaction rates at different crystallographic planes. This process might be similar to anisotropic wet chemical etching of single crystalline Si,[65] which involves chemical reactions that also have dramatically different rates at different crystallographic planes of Si; these different rates are influenced by the bond density at different surfaces (among other factors). Finally, we note that in addition to the kinetics-based explanation, first-principles calculations have indicated that different crystallographic planes of Si react at different electrochemical potentials,[66,67] which may also contribute to anisotropic expansion.

4. Electrochemical Lithiation and Volume Changes in Amorphous Si

The reaction of amorphous Si with Li is different than the crystalline case, as evidenced by the sloping voltage profile for amorphous Si (**Figure 6**, bottom panel).[68] This sloping voltage profile suggests a single-phase lithiation reaction; however,

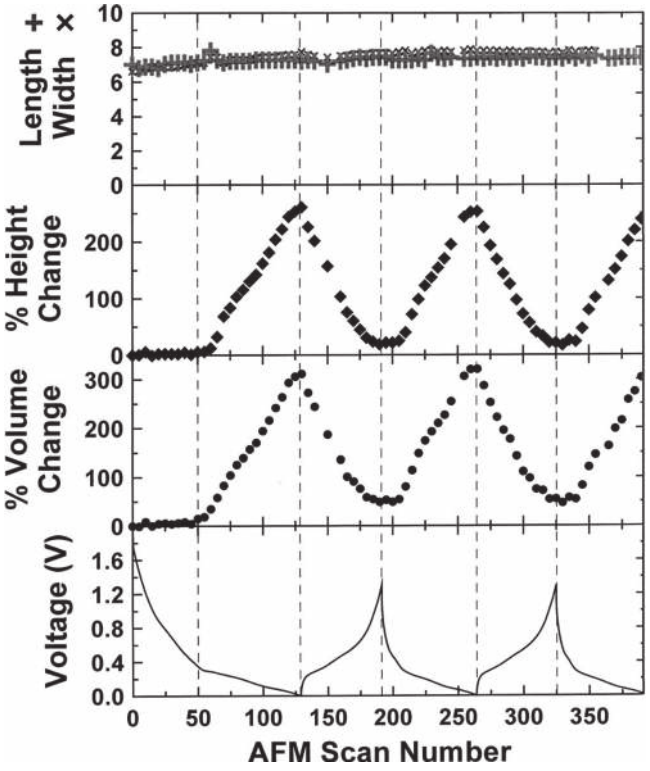

Figure 6. Changes in length, width, height, and volume of a patterned amorphous Si thin film during electrochemical cycling measured with AFM. The corresponding galvanostatic voltage curve is shown below the AFM measurements. These measurements show that the height and volume of the films increase/decrease almost linearly with lithiation/delithiation. Reproduced with permission.[68] Copyright, The Electrochemical Society.

recent experiments have found evidence for two-phase reaction behavior, which will be discussed later. During galvanostatic tests, a slight decrease in voltage about halfway through lithiation is usually observed;[11] this feature has been hypothesized to be due to the local environment surrounding inserted Li atoms.[69,70] Li atoms that are inserted later in the lithiation process are primarily surrounded by other Li atoms, which results in less charge transfer to Si atoms and therefore a slightly lower electrochemical potential.[69] Based on nuclear magnetic resonance (NMR) data and X-ray pair distribution function (PDF) analysis, Key et al. have developed a physical model for amorphous Si lithiation that also helps to explain the slight drop in potential.[39] The Si lattice is broken up into Si clusters by the end of the observed higher voltage process, and further lithiation breaks up these clusters into isolated Si atoms. Late in the lithiation process, the metastable crystalline $Li_{15}Si_4$ phase has been observed to form, similarly as in the lithiation of crystalline Si.[49,71]

Early work on probing the ~300% volume changes in amorphous Si thin films during lithiation/delithiation was carried out by Beaulieu et al.[68] Using in situ atomic force microscopy (AFM), they studied the volume changes of patterned amorphous Si films with thicknesses of 0.3–0.5 μm as the films reversibly reacted with Li. Data from this study are shown in Figure 6;[68] the changes in area, height, and volume of the Si film during the reaction with Li were measured at different points along the voltage profile. The height and volume change linearly with the Li content in the electrode and revert almost to the original values after the first two cycles. Although the height changes dramatically, the lateral dimensions of the patterned films do not noticeably shift; this is probably due to the physical constraint of the substrate. The maximum volume change of the electrode was approximately 300%, which is similar to the theoretical volume change for the transformation of Si to crystalline $Li_{22}Si_5$, 311%.[10] This early study demonstrated the importance of experimentally monitoring volume changes in Si anodes.

As previously mentioned, the sloping voltage profile during lithiation of amorphous Si has led most researchers to conclude that lithiation is a single-phase reaction that does not feature a reaction front. However, recent in situ TEM experiments have revealed more complex two-phase lithiation behavior.[72,73] This distinction is important since the two different reaction mechanisms should theoretically cause different stress evolution and fracture behavior. In one study by McDowell et al., hydrogenated amorphous Si spheres ranging from 400 to 870 nm in diameter were lithiated and delithiated inside a TEM. During lithiation, a phase boundary between the amorphous Li_xSi region and the pure amorphous Si region was clearly observed. High-resolution imaging by Wang et al. has shown that this phase boundary is of nanoscale thickness. Upon analysis, this two-phase behavior was attributed to the rate-limiting effect of Si-Si bond breaking in the amorphous Si, which is similar to the crystalline case. However, the concentration of Li required to break the Si-Si bonds is probably less for the amorphous case than the crystalline case, suggesting a lower activation energy for bond breaking.[72,73] It should also be noted that on subsequent lithiation/delithiation cycles, a single-phase mechanism was observed;[72] this could be a result of Li trapped within the Si or structural changes after delithiation (such as excess Si dangling bonds) that make it kinetically easier to break apart the Si matrix. We speculate that the density of amorphous Si synthesized by various methods may affect the phase behavior during this reaction, and future study is needed. The effects of the two-phase initial lithiation mechanism of amorphous Si on kinetics and fracture behavior will be discussed and compared to the crystalline case in subsequent sections. Finally, as expected, it was found that amorphous Si undergoes isotropic expansion during lithiation because there is no underlying crystallography that affects lithiation.

5. Modeling of Stresses and Fracture during Electrochemical Charge and Discharge

Thus far, we have primarily discussed the phase transformations and volume changes during lithiation and delithiation of nanostructured Si electrodes. However, it is equally important to understand the mechanical stresses that develop due to these volume changes, since the stresses can cause fracture and mechanical degradation. To better understand the relationship between volume changes and fracture during charge and discharge, there have been efforts to model the stresses that arise during lithiation and delithiation of Si structures. The stress states that develop during a single-phase and a two-phase reaction are quite different.[29,62] Since single-phase lithiation/delithiation has been observed to occur upon cycling of Si electrodes, we will first focus on the diffusion-induced stresses (DIS) that have been predicted to occur during single-phase lithiation/delithiation.

5.1. Modeling of Diffusion-Induced Stresses due to Single-Phase Lithiation/Delithiation

Diffusion-induced stresses generally arise from inhomogeneous volume changes resulting from Li concentration gradients within Si. For example, during Li insertion in a spherical particle, the outer shell increases in volume, but the inner region contains less Li and expands to a lesser degree. This strain gradient gives rise to stresses that vary throughout the particle. Diffusion-induced stresses have been described with both analytical and finite element models. Christensen and Newman introduced a continuum model to describe the stresses during volume expansion and contraction of spherical electrode particles, and they primarily focused on carbon insertion compounds that undergo less significant volume changes than Si.[13] An important conclusion was that hydrostatic stress in the outer shell is compressive during Li insertion and tensile during extraction, while the hydrostatic stress in the core of the particle is the opposite. Cheng, Verbrugge, and co-workers have since developed analytical linear elastic solutions for the time-dependent diffusion-induced stresses that arise in solid structures under a variety of conditions.[74–78] They have shown that surface stresses in small nanostructures can affect stress profiles during charging and discharging and have also studied the effects of potentiostatic vs. galvanostatic operation and concentration-

Adv. Mater. 2013,
DOI: 10.1002/adma.201301795

dependent properties on the resulting stresses in electrode particles. Golmon et al. presented simulations describing similar linear elastic deformation and the resultant stresses in spherical Si particles, and they demonstrated that both faster lithiation and larger particle size result in higher maximum tensile stress in the particle interior.[79] In another study, DeLuca et al. developed a linear elastic stress-diffusion model to simulate the stresses present during Li insertion in solid and hollow electrode particle structures.[80] They found that hollow particles experience lower stresses than their solid counterparts, as has also been shown by Yao et al.[21] In addition to these studies, a number of reports have focused on the effect of the large volume changes and associated pressure on the chemical potential and therefore the diffusion of Li.[81–85] The results generally indicate that accounting for pressure-dependent diffusion results in a decrease in predicted stress magnitudes[82,84] caused by gentler Li concentration gradients. Furthermore, one study predicted that under certain charging conditions, diffusion near the surface of a plate electrode might slow to the point that it ceases, an effect called "surface locking."[83] Overall, these studies have largely used linear elastic continuum models to predict diffusion-induced stresses during charge/discharge of electrode structures, and they have shown that the diffusion-induced stresses are rate- and size-dependent.

Recently, in situ experiments measuring the stress evolution in thin-film amorphous Si anodes during lithiation/delithiation have indicated that both yielding and plastic flow occur (these experiments will be discussed later in this review).[86] Inelastic deformation was not considered in many of the aforementioned studies, and it is expected to significantly affect the stresses and fracture behavior of Si electrode structures. Plastic flow can also decrease the energy efficiency of a Li battery, since the rearrangement of atoms dissipates energy but does not significantly contribute to the free energy stored in the material.[86,87] Although the precise nature of plastic deformation on the atomic scale in amorphous Li_xSi has not been experimentally determined, first-principles density functional theory (DFT) simulations have suggested that Li-assisted Si-Si bond breaking and re-forming is largely responsible for plastic flow.[88] This mechanism obviously differs from conventional defect-mediated plasticity in crystalline metals and other materials. A number of models have recently been developed to account for the effects of both elastic and inelastic deformation on the resulting stresses in Si anode structures.[87,89–91] Bower et al. developed a comprehensive finite-strain elastic-plastic model and calculated the coupling between stress and electrochemical potential in a thin film Si anode during cycling, which matched well with experiment.[89] Zhao et al. showed that plastic deformation in a spherical Si particle can significantly decrease the magnitude of the charging rate-dependent stresses that develop. This indicates that materials with lower yield strength are less prone to fracture. Also, during lithiation, plastic deformation was predicted to occur primarily in the outer shell region of the particle where the Li concentration is higher, while plastic deformation does not take place in the particle interior.[87] In another noteworthy study, Cui et al. developed a new formalism for treating the stress-dependent portion of the Li chemical potential, which is designed specifically for more accurately treating the extremely large transformation strains that occur during the Li-Si reaction.[91] This new chemical potential replaces the commonly used result from the important work of Larche and Cahn,[92] which is only accurate for small elastic or transformation strains.[91] Using this new formalism, the authors developed an elastic-plastic model for the stresses that develop due to the diffusion of Li in a spherical amorphous Si particle. Interestingly, the hoop stress at the surface of the particle is predicted to be compressive during the early stages of Li insertion, but at later stages, the hoop stress at the surface becomes tensile due to the expansion of the interior of the particle. This effect could facilitate crack formation at the surface of the particle. This study shows that the unique nature of the physical processes occurring during the electrochemical alloying of Li and Si could require entirely new theoretical frameworks for accurate modeling.

5.2. Modeling of Stress Evolution during Two-Phase Lithiation

The models discussed up to this point were designed to simulate the single-phase reaction in which Li diffuses into or out of a material as determined by Fick's laws. However, during the initial lithiation of crystalline (and amorphous) Si, a different physical process occurs: the unreacted Si is converted to lithiated amorphous Si via a two-phase reaction where the concentration of Li changes over a sharp reaction front. Lithiation and volume expansion occur in a local region near the reaction front, and the overall deformation is controlled by the movement of the reaction front instead of by the diffusion of Li (as in a single-phase reaction). Modeling of two-phase lithiation of crystalline Si particles with different geometries has shown that the stress state is quite different than in the single-phase case.[29,62,93] An important result is that during lithiation of spherical crystalline particles, significant tensile hoop stress can develop at the surface, while hydrostatic compression is present in the crystalline Si core. This stress state is the opposite of the predictions of most models of single-phase lithiation. To illustrate these differences, **Figure 7** shows the hoop stress present in spherical structures that are undergoing single-phase and two-phase lithiation/delithiation processes. During two-phase lithiation of Si particles, the hoop stress at the particle surface arises because the advancing reaction front becomes surrounded by an already-lithiated Li_xSi shell (Figure 7c). Further lithiation at the reaction front causes volume expansion to occur at the front, which pushes out the already-lithiated material near the surface and eventually causes hoop tension. The tensile hoop stress at the surface in the crystalline case can lead to crack initiation at the surface of particles, as confirmed in recent experiments to be discussed later.[29,94]

5.3. Modeling Fracture due to Volume Changes

In addition to studying the stress evolution during charge and discharge of Si, much work has been done to study the mechanisms underlying fracture. This is important because the growth of cracks is influenced by both the stress present and the length scales involved. In early work on fracture in alloying anodes, Huggins and Nix developed a linear-elastic fracture

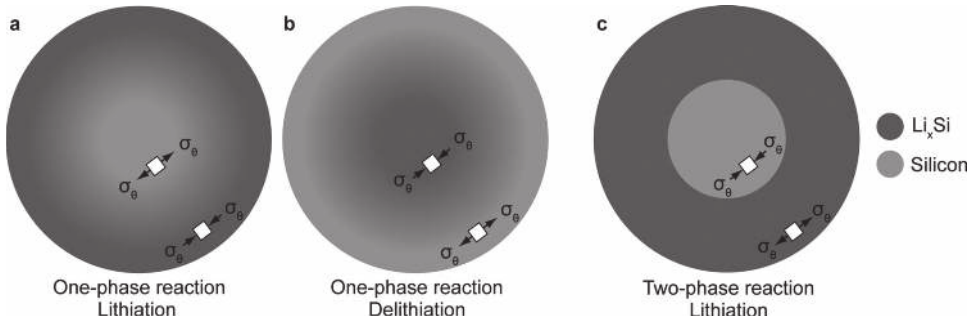

Figure 7. Schematics showing the predicted hoop stress near the center and near the surface of representative spherical particles during single-phase and two-phase lithiation/delithiation processes. The particles are depicted as partially lithiated, with the shade of gray representing the Li concentration. a) Single-phase lithiation, which has been observed to occur in amorphous Si after the first cycle, has usually been predicted to result in compressive hoop stress near the surface and tensile hoop stress in the particle interior.[87] b) Single-phase delithiation, which occurs in lithiated amorphous Si that has not crystallized into the $Li_{15}Si_4$ phase, causes the hoop stress to reverse: there is now tensile hoop stress near the surface and compressive hoop stress in the particle interior. c) Two-phase lithiation, which involves the movement of a sharp reaction front separating two phases with different Li concentrations, causes different stresses to develop than in the single-phase lithiation case. In two-phase lithiation of crystalline Si, the Si core experiences compressive hoop stress, while the lithiated surface region can experience tensile hoop stress.[62]

mechanics model to account for the influence of particle size on fracture.[28] By using a simplified bilayer plate geometry, they predicted that for specific values of fracture toughness and volumetric transformation strain, there should be a critical size below which fracture will not occur in an electrode structure. These calculations are shown in **Figure 8**. This result underpins the experimental search for nanostructured anode materials.

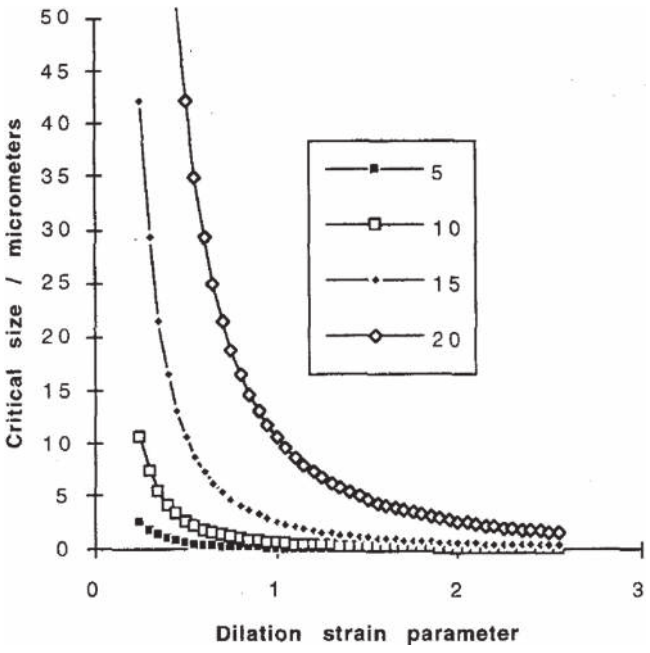

Figure 8. Predicted critical size below which fracture will not occur as a function of dilation strain parameter (equivalent to volume change, $\Delta V/V$) for different values of the fracture toughness of a material. The fracture toughness values, with units of MPa$\sqrt{m}$, are shown in the legend. For a specific value of fracture toughness, the critical size decreases with increasing volumetric strain. This graph shows that for a given material, smaller structures are more resistant to fracture. Reproduced with permission.[28] Copyright 2000, Springer Science and Business Media.

Other more recent studies have built on this fracture mechanics framework by studying crack growth for different geometries and in different materials systems.[95–97] In recent work by Ryu et al., the strain energy release rate associated with advancing a crack was predicted for Si nanowire structures based on a diffusion-induced stress analysis assuming pre-existing flaws; a critical diameter for fracture of ~300–400 nm was predicted.[81] Also, it was shown that the critical diameter is larger for delithiation than for lithiation. Grantab and Shenoy performed finite element simulations to model crack growth in cylindrical Si nanowire structures during cycling, and found that pressure-dependent diffusion significantly alters the global stress and also the local stress at the crack tip.[82] In other work, Cheng and Verbrugge predicted the conditions under which cracks will initiate and propagate in electrode particles.[75,98] Bhandakkar and Gao developed a cohesive zone model to simulate the nucleation of cracks due to diffusion-induced stress in flat and cylindrical structures.[99,100] They also predicted a critical dimension below which an electrode structure would remain crack-free, and they showed that crack nucleation is more likely to occur at the surface of an amorphous Si particle during Li extraction rather than in the interior during Li insertion, even though tensile stresses are present in both cases.

As a final note on modeling efforts, a number of first-principles atomistic models have been used to predict elastic properties of Li-Si alloys.[101–104] These studies generally predict elastic softening with increasing Li content.

6. Experimental Studies of Stress Effects on Fracture and Lithiation

We have previously discussed the models that have been developed to describe the stress evolution during insertion/extraction and how cracks form and grow. Now we focus on experiments that are related to the measurement of stresses and the effect of stress on fracture, electrochemical potential, and lithiation kinetics.

Adv. Mater. **2013**,
DOI: 10.1002/adma.201301795

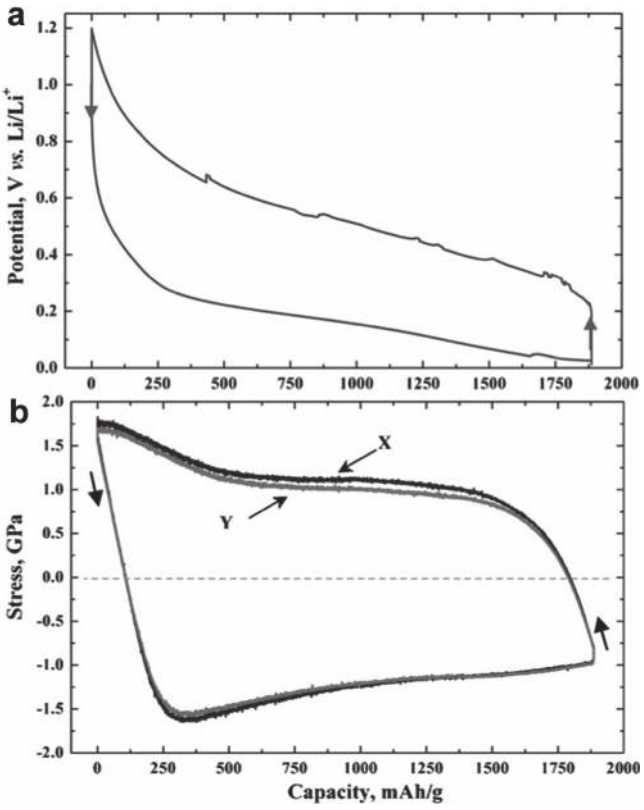

Figure 9. a) Galvanostatic discharge/charge curve of an amorphous Si thin film anode cycled at a rate of C/4. b) Corresponding in situ biaxial stress measurement during the charge discharge process. The arrows in both graphs indicate cycling directions. The two curves X and Y in (b) correspond to horizontal and vertical displacement of adjacent laser spots in the wafer curvature experiment. Reproduced with permission.[86] Copyright 2010, Elsevier.

6.1. Stress in Si Electrodes during Charge and Discharge

A number of studies have used in situ wafer-curvature techniques to monitor the stress evolution in thin Si films during Li insertion/extraction. An early study was performed by Lee et al.[105] More recently, Sethuraman et al. performed similar measurements, and compressive and tensile flow stresses in excess of 1 GPa were found during Li insertion and extraction (respectively) in amorphous Si films.[86] These data are shown in **Figure 9**. Figure 9a shows the galvanostatic discharge/charge curves for a Si film, and Figure 9b shows the simultaneously measured biaxial stresses in the film. The stress plot in Figure 9b shows that during the initial stages of lithiation, the film undergoes elastic loading. At a capacity of about 300 mAh g^{-1}, the film yields and plastic deformation begins to occur, with plastic flow continuing throughout the rest of lithiation. Upon delithiation, similar behavior occurs, but with tensile instead of compressive biaxial stresses. These important measurements reveal the existence of large flow stresses and extensive plastic flow behavior during phase transformations. Related work has shown that the nominal flow stress is greater for thinner films.[106] Other studies have shown that by patterning thin (50nm) amorphous Si films into islands less than ~7 μm in width, the stress that arises during lithiation/delithiation remains elastic.[107,108] In addition, continuous films were observed to fracture during delithiation, while the patterned films did not.[108] In another study, the stress was monitored as a crystalline Si wafer was lithiated via the two-phase crystalline/amorphous reaction mechanism previously discussed. The compressive stress in the amorphous Li_xSi region remained at a constant value of ~0.5 GPa during lithiation, which indicates that the lithiated Si was undergoing plastic flow at this stress level. During delithiation, the measured biaxial stress rapidly became tensile. Fracture and a sudden drop in the magnitude of the tensile stress were both observed near the end of delithiation.[38] Taken together, this important research on mechanical behavior has shed light on the strength, flow behavior, and damage evolution of Si during cycling.

6.2. Relating Stress to Electrochemical Potential

Since relatively large (~GPa level) hydrostatic stresses have been shown to exist in Si anodes during Li insertion/extraction, this influences the Gibbs free energy of the reaction and therefore the measured electrochemical potential.[89,109,110] Based on the stress experiment detailed in Figure 9, Sethuraman et al. employed the Larche-Cahn chemical potential to predict the magnitude of stress-potential coupling in lithiated Si.[109] It was estimated that a biaxial stress of 1 GPa would change the measured electrochemical potential by 62 mV in a thin-film geometry, and experimental measurements show that the coupling could be as high as 100-125 mV GPa^{-1}. This result indicates that stress in Si anodes contributes to the voltage hysteresis present during charging and discharging, since the compressive stress during lithiation would decrease the voltage from the equilibrium value and the tensile stress during delithiation would increase it.[109] In general, voltage hysteresis is detrimental since it results in lower energy efficiency, and it also makes it difficult to determine the state of charge of the battery. As such, it is important to determine the factors influencing the hysteresis, and this work provides valuable insight into the role of mechanical stress in contributing to the voltage hysteresis. Other studies in this area have focused on the effects of stress and physical constraint on the equilibrium Li concentration during Li insertion and extraction.[110,111]

6.3. The Effect of Stress on the Kinetics of Lithiation

In addition to the aforementioned stress effects, it has also been predicted that stress can alter the lithiation rate in individual nanostructures. In particular, the large stresses that develop at the Si/Li_xSi interface during lithiation of crystalline Si nanoparticles or nanowires can influence the nature of the reaction in a unique way; specifically, the stress acts to gradually decrease the thermodynamic driving force for lithiation as the reaction progresses.[62] This effect results from the spherical geometry of nanoparticles. An in situ TEM experimental study by McDowell et al. demonstrated the effects of stress on the lithiation reaction by analyzing the real-time lithiation of individual Si nanoparticles.[51] It was found that the reaction

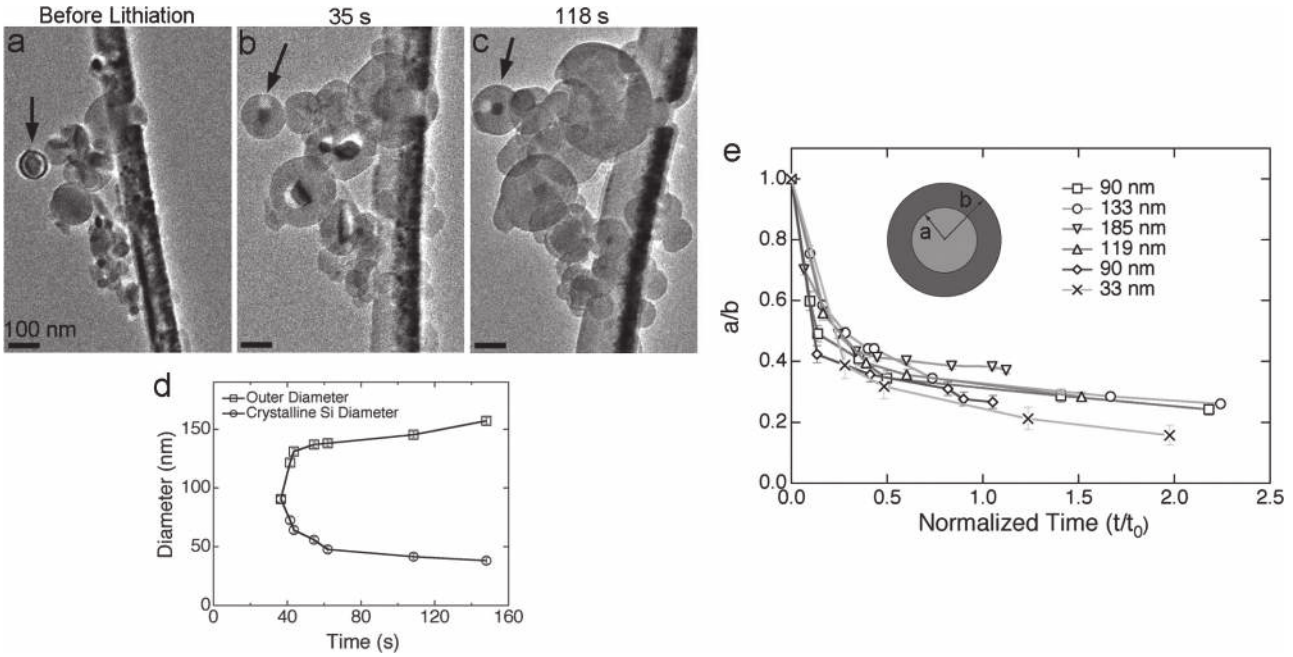

Figure 10. Real-time measurement of the extent of lithiation with time in individual crystalline Si nanoparticles. a-c) In situ TEM images showing a group of nanoparticles being lithiated. The particles are attached to a Cu-coated Si nanowire from which the Li flows. In (b), the particles are partially lithiated, and the crystalline Si core/amorphous Li_xSi shell structure is evident in many particles (the crystalline Si core is darker). The arrows in these images mark the particle that is analyzed in panel (d). d) Measurement of the outer diameter and crystalline core diameter as a function of time during lithiation for the particle marked with an arrow in (a-c). Initially the reaction proceeds quickly, but the reaction front slows significantly as the particle is lithiated. e) This plot shows the extent of lithiation (quantified as the a/b ratio, where b is the outer radius and a is the core radius) as a function of normalized time t/t_o for six particles from the group shown in panels (a-c). "Normalized time" is given by t/t_o, where $t_o = b_o/v_o$ (b_o is the initial radius and v_o is the initial reaction front velocity for each particle). This plot shows that particles of all sizes exhibit reaction front slowing when they are lithiated to a similar a/b ratio. This is evidence for a stress effect on the driving force for the reaction, since the hydrostatic stress in the particles theoretically does not depend on particle size but only on the extent of lithiation.[62] Reproduced with permission.[51] Copyright 2012, WILEY-VCH Verlag GmbH & Co.

front slows significantly as the crystalline Si core is consumed, whereas traditional reaction front-controlled kinetics predicts a constant lithiation rate. Data from this study are shown in **Figure 10**. Analysis of the data strongly suggests that increasing hydrostatic compression near the interface during lithiation causes the slowing reaction rate.[51] A subsequent study has shown that similar behavior occurs in nanowires, where the cylindrical shape results in similar stresses as the spherical nanoparticles.[112] In both cases, the reaction front slowing arises due to the extreme volumetric expansion at the two-phase interface, and as such it is quite different from other battery materials systems. This behavior also has direct consequences for battery operation, since the slowing of the reaction could limit charging rates.

As previously discussed, in situ TEM experiments have shown that the first lithiation of amorphous Si occurs via a two-phase reaction in a similar manner as crystalline Si.[72] This should result in similar stress evolution during lithiation, which might lead one to expect slowing of the reaction front during lithiation of amorphous Si spheres. However, direct measurements have shown that the reaction front does not slow in amorphous Si spheres;[72] instead, the reaction front proceeds approximately linearly with time. This difference suggests that the hydrostatic stress in amorphous Si spheres is lower than that in crystalline Si spheres during lithiation, which is consistent with the observation of less volume expansion at the reaction front for amorphous Si.[73]

6.4. Fracture due to Li Insertion/Extraction

The stresses that exist in amorphous Si thin films during cycling are due both to the constraint of the substrate and to Li concentration gradients in the film itself. Many studies have shown that amorphous Si films over ~100 nm in thickness fracture upon delithiation due to tensile stresses.[113,114] Depending on the substrate material, very thin films (<50 nm) have been reported to avoid fracture/delamination and maintain high capacity over thousands of cycles;[115] this can be explained by the lower strain energy available to drive crack propagation in these thin films.[113] A recent study has sought to reduce the stresses in thicker films by using Si films placed on soft poly(dimethylsiloxane) (PDMS) substrates as anodes.[116] In this case, the PDMS substrate can deform during volume expansion and contraction, which reduces the stress in the Si film and allows for stable cycling. This demonstrates that clever engineering can mitigate some of the problems associated with stresses and fracture in Si.

DOI: 10.1002/adma.201301795

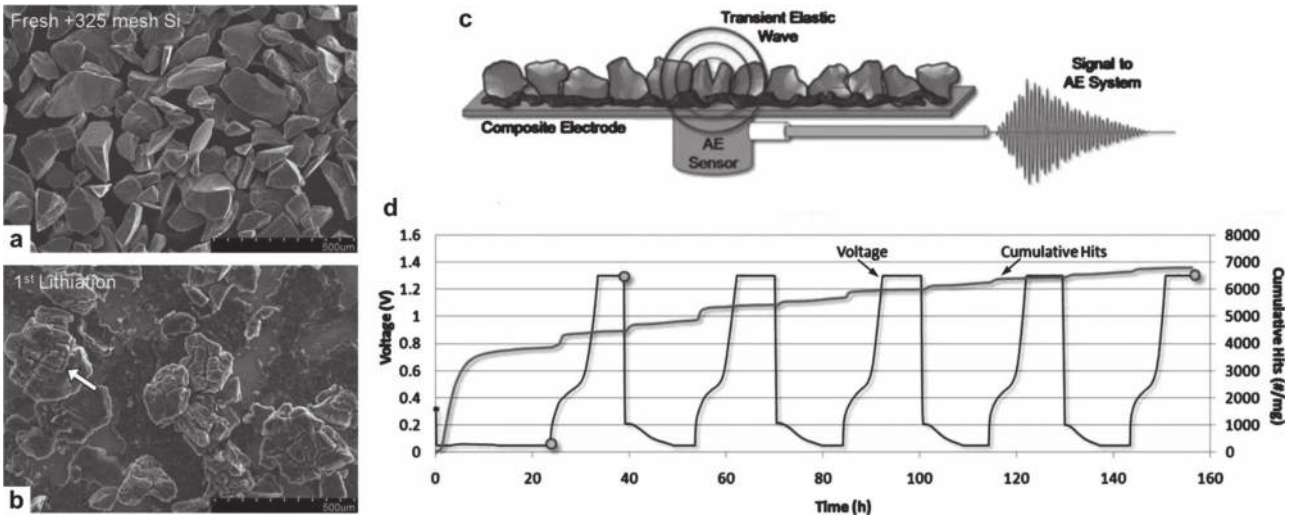

Figure 11. a,b) SEM images of 325 mesh crystalline Si particles before (a) and after (b) lithiation. Cracks on the particle surface were observed after lithiation. c) Schematic showing the setup of the acoustic emission experiment: elastic waves produced by fracture events propagate through the electrode until reaching the acoustic emission sensor, which sends a voltage signal to a computer for recording and processing. d) Acoustic emission signal measured during galvanostatic cycling of a crystalline Si particle electrode. Cumulative hits and voltage vs time are shown. The first lithiation shows the greatest number of fracture events. Reproduced with permission.[37] Copyright, The Electrochemical Society.

Fracture has also been investigated in Si structures without thin film morphologies. In a series of interesting experiments, the acoustic emission signal from crystalline Si particle electrodes was monitored during cycling.[37,117] In these experiments, a piezoelectric sensor on the back of a Si particle electrode was used to record mechanical vibrations emanating from the fracture of the particles. Acoustic events corresponding to particle fracture were detected throughout cycling, with an increased frequency of fracture events during the initial lithiation of crystalline Si compared to later cycles. The authors also performed SEM, and cracks on the surface of the particles were observed after the first lithiation. After the first delithiation, the particles had a similar appearance but the cracks were less severe due to particle shrinkage. After five cycles, a multitude of smaller cracks appeared in the large fissures and many of the initial particles had been pulverized into smaller particles. This data is shown in **Figure 11**.

It is evident from these experiments that fracture of crystalline Si particles during the first lithiation is severe and could contribute to the first cycle irreversible capacity loss commonly observed in Si electrodes, but until recently this phenomenon was not understood at the single-particle level. To explore this issue, Liu et al. used in situ TEM techniques to visualize fracture during the lithiation of crystalline Si particles with sizes ranging from ~20 nm to hundreds of nm.[29] It was found that cracks initiate at the surface of particles during the movement of the reaction front into the particle. In addition, the critical particle size for fracture was estimated to be about 150 nm based on the experiments. Crack initiation at the surface is a direct consequence of the stress state that exists during lithiation of crystalline particles. As previously discussed, both Liu et al. and Zhao et al. have developed models to describe stress evolution during lithiation of crystalline spherical particles.[29,62] The relevant result is that due to propagation of the sharp reaction front separating crystalline Si from highly lithiated amorphous Si, tensile hoop stresses develop at the surface, which results in the observed fracture. This differs from what is expected in a single-phase reaction, where the surface region has usually been predicted to be under hoop compression during lithiation instead of tension (for reference, Figure 7 has schematics illustrating the hoop stress predicted for single-phase and two-phase reactions in particles).[87]

Ex situ work by our group has shown that crystalline Si nanopillars also fracture at the surface during lithiation, and we have examined the influence of crystalline orientation and anisotropic volume expansion on fracture.[94] In this study, we fabricated <100>, <110>, and <111> axially oriented nanopillars on Si wafers. The diameter of the pillars ranged from ~150 nm to ~400 nm, and the height of the pillars was a few microns. After lithiation, SEM revealed that many pillars had surface cracks, and the occurrence of fracture was found to be dependent on size and lithiation rate. Fracture was observed in ~90% of nanopillars that were initially 360 nm in diameter, while only ~5% of nanopillars that were initially 140 nm in diameter fractured. These values varied only about 5% with the voltage sweep rate. For nanopillars of an intermediate size (240 nm), however, the fraction of nanopillars with cracks increased from ~1% at slow lithiation rates to about ~20% at fast rates. This seems to suggest a lithiation rate-dependence on the stress evolution at the surface of the pillars, but more work needs to be done to further clarify this effect.

Another important conclusion of this study is that anisotropic expansion during lithiation of crystalline Si nanostructures influences the location of cracks. This is demonstrated in **Figure 12**, which shows crack location statistics in lithiated nanopillars with different axial orientations.[94] For pillars with all three axial orientations, it is clear that the cracks are primarily located between neighboring {110} planes. Recalling that the

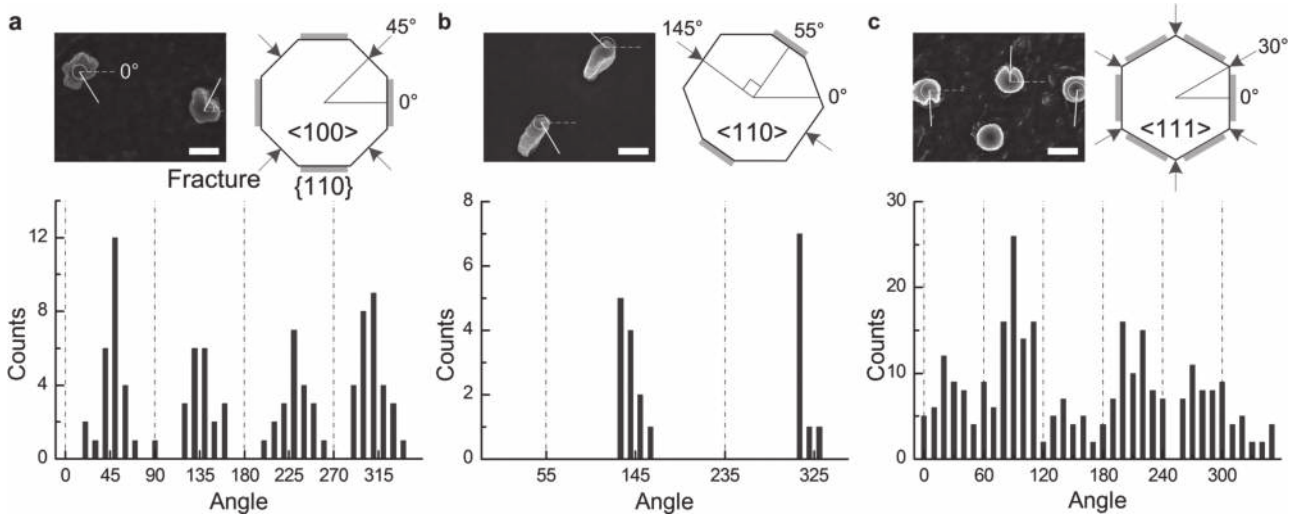

Figure 12. Statistical study of the fracture locations at the surface of lithiated Si nanopillars with different axial orientations. Each panel shows an example SEM image of fractured pillars, a schematic of the pillar cross-section, and a compilation of fracture location data presented as a column chart. The data were compiled by examining many top-down SEM images and measuring the angle from an arbitrary reference point to the fracture location, as shown in the SEM images and schematics. The dashed lines in the inset SEM images indicate the reference point (0°), and the solid lines show the location of the cracks; the angular location of the cracks is measured between these lines. The thicker highlights in the schematic views and the dashed lines in the column charts indicate the angular location of the {110} surfaces on the sidewalls of the pillars. Arrows point to fracture sites. a) Pillars with <100> axes expand preferentially at the four lateral {110} surfaces (0, 90, 180, and 270° in the figure), and the four most common fracture sites are located at the {100} lateral surfaces (45, 135, 225, and 315° in the column chart). b) Pillars with <110> axes expand preferentially at the two lateral {110} surfaces (55 and 225° in the figure), and the two most common fracture sites are at the lateral {100} surfaces (145 and 325° in the column chart). c) Pillars with <111> axes have six lateral {110} surfaces that expand preferentially (0, 60, 120, 180, 240, and 300° in the figure), and the most common fracture sites are the {112} lateral surfaces that are positioned between neighboring {110} surfaces (30, 90, 150, 210, 270, and 330° in the column chart). Overall, these data show that nanopillars of all orientations consistently fracture at surface locations that lie midway between lateral planes that undergo preferential lithiation, as shown by the arrows in the schematics. Scale bars in the SEM images are 1 μm. Reproduced with permission.[94] Copyright 2012, National Academy of Sciences U.S.A.

{110} planes are the locations of preferential lithiation and expansion, this suggests that anisotropic expansion results in stress intensification at the surface between the {110} planes, which causes fracture. Another in situ study on <112> axially-oriented Si nanowires has also shown that anisotropic expansion can result in fracture.[58] In this case, some nanowires were observed to develop cracks along the axis during lithiation.

In addition to these studies, we have also performed in situ TEM experiments that reveal in real-time the effect of anisotropic expansion on fracture locations.[51] In this case, we studied crystalline Si particles instead of one-dimensional structures. **Figure 13** shows a series of TEM images taken from a video of the lithiation process of a nanoparticle with an initial diameter of ~480 nm. In this experimental configuration, lithiation occurs at all surfaces relatively uniformly since surface diffusion of Li has been confirmed to be much faster than bulk diffusion.[29,50,58] As lithiation progresses in this particle, the darker-contrast crystalline core region shrinks as the amorphous Li_xSi shell grows (Figures 13b,c). The crystalline core also becomes faceted (Figures 13c,d), as discussed previously. After 205 sec of lithiation (Figure 13c), a set of two protruding facets that forms a triangular shape is seen on the left side of the crystalline core during lithiation. Assuming the two facets are {110} planes, the shape of this protrusion could be a result of the extensive twinning evident in this particle; it is also possible that this protrusion is a smaller secondary crystal separated from the larger crystal by a grain boundary. Lithiation is occurring at this protrusion primarily at the top and bottom facets, while the tip of the protrusion remains sharp. As such, the lithiated shell directly to the left of the protrusion tip is thinner than in any other location since less extensive lithiation is occurring at the tip than at the preferentially-lithiated facets. In Figure 13e, fracture is observed to initiate at the surface of the partially lithiated particle directly to the left of the tip of the crystalline protrusion. The location of fracture indicates that the preferential lithiation and concurrent plastic flow of material above and below the protrusion tip result in intensified tensile hoop stress at the particle surface directly to the left of the protrusion. This is very similar to the ex situ results observed after lithiation of nanopillars; in both cases, fracture occurs at the surface between angled surfaces of preferential lithiation.[94] After the particle fractures in Figure 13e, the remaining crystalline core of the particle quickly becomes lithiated and the crack grows across the entire particle, as shown in Figure 13f. The destruction of the original particle morphology and the separation into two pieces is an example of how fracture could lead to loss of electrical contact in individual particles. As mentioned before, this is thought to be a mechanism of fracture-induced capacity loss in Si electrodes and could help explain why crystalline particle-based electrodes are usually observed to exhibit relatively large irreversible capacity loss on the first cycle.[12,17,36]

DOI: 10.1002/adma.201301795

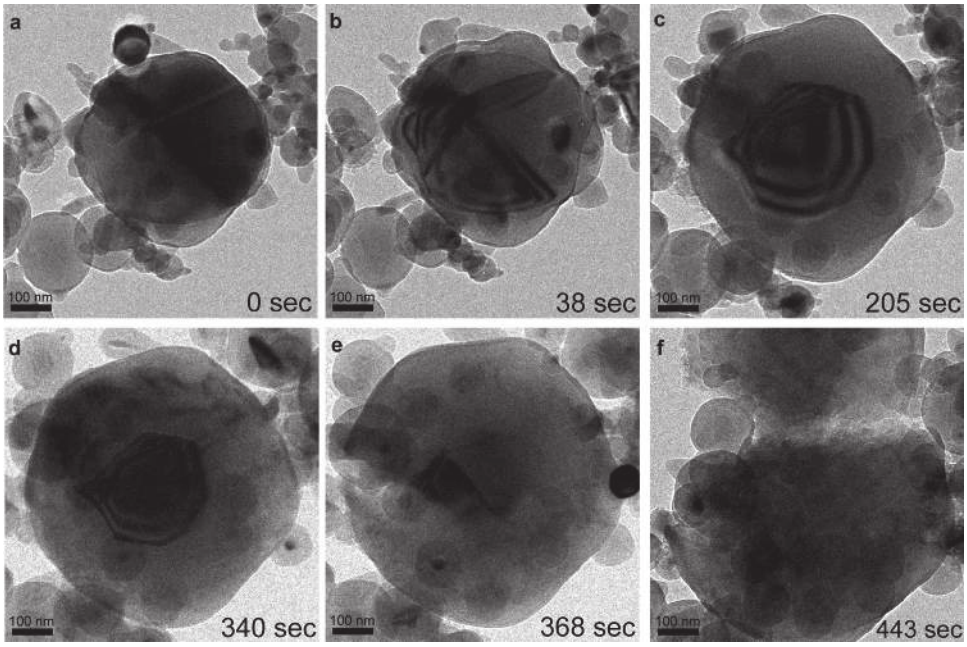

Figure 13. Series of in situ TEM images showing the lithiation of a ~480 nm diameter crystalline Si nanoparticle. The time from the beginning of the experiment is displayed in the bottom right of each image. In this experimental setup, the visible particles are in physical contact with each other, and Li atoms diffuse through the smaller particles to the left of the large particle to react with the larger particle. a) The large particle has just begun to undergo lithiation. b) Amorphous Li_xSi regions (lighter contrast) are visible surrounding the darker crystalline Si core. The angled lines in the core are twin defects. c) The crystalline core has shrunk significantly, and it is surrounded by an amorphous Li_xSi shell. The core is faceted due to anisotropic expansion. Also, a set of two protruding facets is visible on the left side of the crystalline core. d) The particle before crack initiation. The lithiated shell has transformed to the $Li_{15}Si_4$ phase. e) With further lithiation, a crack initiates on the left surface of the particle directly adjacent to the crystalline protrusion. Anisotropic expansion above and below the protrusion results in tensile stress concentration at this surface location. f) After fracture, the crack grows as the remaining crystalline core is lithiated, causing the particle to almost completely separate into two pieces. Reproduced with permission.[51] Copyright 2012, WILEY-VCH Verlag GmbH & Co.

Finally, we note that work has also been devoted to developing surface coatings that do not fracture upon the expansion and contraction of Si nanoparticles or nanowires. Certain surface coatings, such as carbon or Cu, can ideally promote stable solid-electrolyte interphase (SEI) growth and result in higher Coulomb efficiency,[118] but many surface coatings applied directly to Si structures will fracture due to volume expansion of Si upon lithiation, as demonstrated by in situ TEM experiments.[50] To bypass this problem, hollow nanostructures of a few different types have recently been developed that all feature a surface coating and empty space into which Si can expand.[18,22,23,119] During lithiation, the Si can expand into the empty space without significantly deforming the surface layer (depending on the mechanical properties and thickness of the coating), which results in a static surface exposed to the electrolyte on which a stable SEI can grow.[120] This design principle, which was guided by knowledge gained from fundamental studies, has resulted in half-cells with stable discharge capacity over hundreds and even thousands of cycles.[22]

7. Measurements of Mechanical Properties of Li-Si Alloys

Since the mechanical properties of Li-Si alloys play a significant role in degradation processes, comprehensive knowledge of these properties is necessary. For Li-Si alloys, measuring the mechanical properties has been a challenge because the materials are unstable in air. Recently, however, there have been a few studies reporting mechanical properties of lithiated Si. Using wafer-curvature techniques, Sethuraman et al. measured the biaxial modulus of thin amorphous Si films during electrochemical lithiation, and found that the biaxial modulus varies from ~70 GPa for lightly lithiated Si to ~35 GPa for highly lithiated Si.[121] It is important to take these differences into account in the modeling of stresses. In two other studies by Ratchford et al., nanoindentation was used on bulk alloy samples of $Li_{12}Si_7$ and $Li_{22}Si_5$ to determine Young's modulus, and values of 52.0 ± 8.2 GPa and 35.4 ± 4.3 GPa were reported, respectively.[122,123] Additionally, Hertzberg et al. studied electrochemically lithiated Si films with nanoindentation, and reported the Young's modulus and hardness as a function of extent of lithiation.[124] They also showed a deviation from the rule of mixtures for Young's modulus measurements, which could be explained by changes in the local environment of Si and Li atoms during lithiation. The reported hardness values in the study more closely follow a rule of mixtures, with the hardness of $Li_{15}Si_4$ reported as 1.5 ± 0.8 GPa. In addition to these measured properties, studies have shown that the lithiation of Si causes a transformation from brittle behavior to a material that can undergo significant plastic flow.[86,125] This transformation highlights the importance of understanding the mechanical properties at various Li

compositions. Finally, the mechanical properties of lithiated or delithiated nanowires have been examined recently with tensile tests and AFM indentation tests; these experiments represent novel approaches for probing the mechanical response of individual nanostructures.[126–128]

8. Experimental Studies of Physical Transformations in Other Nanostructured Anode Materials

Due to the particular promise of Si as an anode material, the reaction processes in the Li-Si system have been widely studied, as detailed in this review. Single-nanostructure characterization techniques have been vital for probing the nanoscale details of the Li-Si reaction; this type of study has led to greater understanding of phase transformations, mechanical degradation, and reaction kinetics. In addition to Si, however, there are a number of other promising anode materials that have been studied in recent years, and experiments have begun to reveal the wide variety of nanoscale reaction mechanisms that take place in different materials. These different mechanisms require the development of new models for stress evolution to better understand the mechanics of these systems. This section discusses experimental results (with a focus on single-nanostructure studies) related to the reaction and mechanical degradation mechanisms of other novel anode materials.

Germanium and tin are group IV elements along with Si, and they can both alloy with a high concentration of Li (the specific capacities of Ge and Sn are 1623 and 994 mAh g^{-1}, respectively). Ge has been the subject of a few different in situ TEM studies, and interestingly, although both Ge and Si have diamond cubic crystal structures, there are important differences in the reaction behavior. First, the two-phase lithiation of crystalline Ge has been shown to be isotropic,[129–131] in contrast to the significant anisotropic expansion observed during lithiation of Si. This has important ramifications for lithiation-induced fracture of Ge nanostructures. In section 6, it was shown that anisotropic expansion of Si nanostructures causes fracture to occur between crystallographic planes where preferential lithiation takes place; this is due to heightened tensile stress at these locations. The isotropic of lithiation of Ge avoids these stress concentrations, which results in a larger critical size for fracture of Ge nanoparticles.[129] Another feature of the Li-Ge reaction is that after delithiation, highly porous amorphous Ge has been observed to form.[131] Upon cycling, the pores disappear and reform; this is in contrast to the behavior observed in Si nanowires, which become porous over tens of cycles.[132]

A few studies have examined the morphological evolution of Sn particles with cycling. One ex situ study concluded that 50 nm Sn particles undergo fracture during long term cycling, which indicates that Sn may be less mechanically stable than Si.[133] In another study, monodisperse Sn nanocrystals with a diameter of about 10 nm were observed with TEM before and after lithiation/delithiation.[134] Interestingly, there was evidence of mechanical damage and fracture even in these small crystals, which again suggests differences in mechanical stability of Sn compared to Si. Other work has focused on using in situ AFM to probe volume changes in patterned Sn films, and it was found that volume changes were not completely reversible with cycling (as they were in similar experiments with Si films).[135] Finally, the transformations during lithiation/delithiation of larger Sn particles (~5 microns) have been studied with in situ transmission X-ray microscopy (TXM).[136,137] Radial fracture was observed to occur during lithiation, and the particles became porous after delithiation. The fracture behavior is similar to that observed for Si nanostructures, although the Sn particles were much larger.

In addition to these alloying anode materials, other in situ experiments have revealed the nanoscale reaction mechanisms of oxide-based anode materials, such as SnO_2 and ZnO.[138–141] This type of material is lithiated through a conversion process where in the early stages of lithiation the metal oxide is converted to Li_2O and the pure metal, and then the metal is lithiated to form a Li-metal alloy if it is active for Li alloying. During the lithiation of SnO_2 nanowires, the SnO_2 is initially converted to amorphous Li_2O and nanocrystalline Sn.[140,142] A reaction front separates the crystalline SnO_2 from the Li_2O/Sn, and ahead of this reaction front there is a ~200 nm wide "dislocation cloud" that moves through the SnO_2 crystal. This indicates that severe plastic deformation occurs both in the SnO_2 crystal and the lithiated amorphous region, which is different than the case of Si lithiation, where dislocations have not been observed in the Si lattice. Additionally, it has been found that surface coatings can act as a constraint to control the expansion anisotropy during SnO_2 lithiation;[143] this also contrasts with Si,[50] where the expansion anisotropy is controlled by the crystallography of the Si lattice.[56–58] These findings show that both the reaction mechanism and the mechanics of volume expansion are quite different for Si and SnO_2. In addition to these tests on SnO_2 nanowires, in situ TEM results of the lithiation and cycling of ZnO nanowires have been reported.[139] The lithiation of ZnO proceeds by a different mechanism than SnO_2; instead of the dislocation-mediated plasticity observed in SnO_2, the ZnO nanowires undergo significant cracking and fracture during lithiation, which causes mechanical damage to the nanowire that remains during cycling. Overall, these results have begun to reveal the wide variety of different reaction pathways possible for the lithiation of anode materials, and they indicate that there is more to work to be done to uncover and understand the reaction of Li with other electrode materials.

As a final note regarding novel characterization methods, Balke and Kalinin et al. have developed an interesting scanning probe technique, termed electrochemical strain microscopy, for investigating volume changes and ionic transport in thin film electrodes.[144,145] This technique has proven useful for mapping Li flow in $LiCoO_2$ and Si films and for determining the effect of defects on Li diffusion, and it will surely be used in the future to study a variety of novel battery materials.

9. Conclusions

With the intense recent interest in developing new high-capacity Li battery electrode materials, Si has received much research attention. The lithiation of Si is fundamentally different from traditional intercalation anodes: Li alloys with Si, causing 300% volume expansion in the process. As demonstrated by the studies discussed herein, the development of

Adv. Mater. 2013,
DOI: 10.1002/adma.201301795

high-capacity alloying anode materials such as Si requires not only traditional electrochemical experiments, but also experiments designed to monitor the interrelated effects of volume expansion/contraction, deformation, stress evolution, and fracture on the mechanical integrity and electrochemical performance of these materials. For Si, such experiments and modeling have revealed a wealth of information, including the effect of crystallinity on volume expansion, the details of mechanical stress evolution and its relation to electrochemical potential, and dynamic fracture information. These data are useful for understanding the physical processes occurring in an electrode structure during electrochemical reactions, and they will hopefully guide future Si electrode development and also the development of other alloying anode materials.

Although much has been learned about the Li-Si alloying reaction, many topics in this area are as yet unstudied. Some important future research areas are detailed here.

1. Most of the studies mentioned in this review deal with the electrochemical reaction of individual Si structures; however, it is also important to examine the interactions between particles and the mechanical degradation of electrode frameworks on a larger (μm to cm) scale. This will allow for the correlation of single particle deformation to the mechanical integrity and electrochemical performance of the electrode framework.
2. It is necessary to study in detail the effects of volume expansion on SEI growth. SEI films have been shown to become very thick on nanostructured anodes; this is presumably because volume expansion/contraction can rupture already-grown SEI and expose new Si surfaces to the electrolyte, where new SEI forms. Thicker SEI increases ionic resistance and can cause electrical isolation of fractured particles, which can lead to capacity degradation. Although some progress has been made in this area,[22] it would be useful to understand exactly how SEI growth occurs on different alloying anode nanostructures so new methods can be developed to promote stable SEI growth.
3. The bulk of this review is concerned with the physical and chemical transformations during the lithiation/delithiation of Si. A large number of studies have focused on Si due to its attractive properties as an anode material, and a good deal of knowledge about this reaction has been generated. However, as detailed in section 8, experimental studies on the nanoscale reaction processes in other nanostructured electrode materials have also begun to emerge. In most cases, different materials exhibit different reaction mechanisms, indicating that it is important to understand these differences through more experiments and modeling.
4. Complete knowledge of the mechanical behavior of lithiated Si is necessary to understand and predict structural deformation during lithiation/delithiation. While some mechanical properties have already been measured, important questions remain. For instance, viscoplastic flow behavior and related mechanisms would be interesting to characterize.

The extent of recent research and the progress made in understanding the electrochemistry and materials science of Si anodes for Li batteries, along with improvements in performance, suggest that there is a bright future for the commercial prospects of this material. With more work towards fundamental understanding and electrode development, Li-ion batteries with higher capacity and long cycle life could be realized.

Acknowledgements

This article is part of an ongoing series celebrating the 25th anniversary of *Advanced Materials*. This work is supported by the U.S. Department of Energy, Assistant Secretary for Energy efficiency and Renewable Energy, Office of Vehicle Technologies of the U.S. Department of Energy under Contract No. DE-AC02-05CH11231, Subcontract No. 6951379 under the Batteries for Advanced Transportation Technologies (BATT) Program. M.T.M. acknowledges support from the Chevron Stanford Graduate Fellowship, the National Defense Science and Engineering Graduate Fellowship, and the National Science Foundation Graduate Fellowship. W.D.N. gratefully acknowledges support of the Office of Science, Office of Basic Energy Sciences, of the US Department of Energy under contract no. DE-FG02-04ER46163.

Received: April 22, 2013
Published online:

[1] J. M. Tarascon, M. Armand, *Nature* **2001**, *414*, 359–367.
[2] M. S. Whittingham, *Proc. IEEE* **2012**, *100*, 1518–1534.
[3] R. Marom, S. F. Amalraj, N. Leifer, D. Jacob, D. Aurbach, *J. Mater. Chem.* **2011**, *21*, 9938–9954.
[4] USABC Electric Vehicle Battery Test Procedures Manual, U.S. Advanced Battery Consortium, 1996.
[5] D. Larcher, S. Beattie, M. Morcrette, K. Edstroem, J. C. Jumas, J. M. Tarascon, *J. Mater. Chem.* **2007**, *17*, 3759–3772.
[6] U. Kasavajjula, C. S. Wang, A. J. Appleby, *J. Power Sources* **2007**, *163*, 1003–1039.
[7] W.-J. Zhang, *J. Power Sources* **2011**, *196*, 13–24.
[8] M. N. Obrovac, L. Christensen, *Electrochem. Solid-State Lett.* **2004**, *7*, A93–A96.
[9] P. Limthongkul, Y. I. Jang, N. J. Dudney, Y. M. Chiang, *Acta Mater.* **2003**, *51*, 1103–1113.
[10] L. Y. Beaulieu, K. W. Eberman, R. L. Turner, L. J. Krause, J. R. Dahn, *Electrochem. Solid-State Lett.* **2001**, *4*, A137–A140.
[11] M. N. Obrovac, L. J. Krause, *J. Electrochem. Soc.* **2007**, *154*, A103–A108.
[12] C. K. Chan, H. L. Peng, G. Liu, K. McIlwrath, X. F. Zhang, R. A. Huggins, Y. Cui, *Nat. Nanotechnol.* **2008**, *3*, 31–35.
[13] J. Christensen, J. Newman, *J. Solid State Electrochem.* **2006**, *10*, 293–319.
[14] C. J. Wen, R. A. Huggins, *J. Solid State Chem.* **1981**, *37*, 271–278.
[15] S.-C. Lai, *J. Electrochem. Soc.* **1976**, *123*, 1196–1197.
[16] H. Kim, M. Seo, M. H. Park, J. Cho, *Angew. Chem., Int. Ed.* **2010**, *49*, 2146–2149.
[17] I. Kovalenko, B. Zdyrko, A. Magasinski, B. Hertzberg, Z. Milicev, R. Burtovyy, I. Luzinov, G. Yushin, *Science* **2011**, *334*, 75–79.
[18] B. Hertzberg, A. Alexeev, G. Yushin, *J. Am. Chem. Soc.* **2010**, *132*, 8548.
[19] A. Magasinski, P. Dixon, B. Hertzberg, A. Kvit, J. Ayala, G. Yushin, *Nat. Mater.* **2010**, *9*, 353–358.
[20] L.-F. Cui, Y. Yang, C.-M. Hsu, Y. Cui, *Nano Lett.* **2009**, *9*, 3370–3374.
[21] Y. Yao, M. T. McDowell, I. Ryu, H. Wu, N. A. Liu, L. B. Hu, W. D. Nix, Y. Cui, *Nano Lett.* **2011**, *11*, 2949–2954.
[22] H. Wu, G. Chan, J. W. Choi, I. Ryu, Y. Yao, M. T. McDowell, S. W. Lee, A. Jackson, Y. Yang, L. Hu, Y. Cui, *Nat. Nanotechnol.* **2012**, *7*, 310–315.

[23] N. Liu, H. Wu, M. T. McDowell, Y. Yao, C. Wang, Y. Cui, *Nano Lett.* **2012**, *12*, 3315–3321.
[24] T. H. Hwang, Y. M. Lee, B.-S. Kong, J.-S. Seo, J. W. Choi, *Nano Lett.* **2011**, *12*, 802–807.
[25] J. R. Szczech, S. Jin, *Energy Environ. Sci.* **2011**, *4*, 56–72.
[26] T. Song, J. L. Xia, J. H. Lee, D. H. Lee, M. S. Kwon, J. M. Choi, J. Wu, S. K. Doo, H. Chang, W. Il Park, D. S. Zang, H. Kim, Y. G. Huang, K. C. Hwang, J. A. Rogers, U. Paik, *Nano Lett.* **2010**, *10*, 1710–1716.
[27] Y. Yu, L. Gu, C. B. Zhu, S. Tsukimoto, P. A. van Aken, J. Maier, *Adv. Mater.* **2010**, *22*, 2247–2250.
[28] R. A. Huggins, W. D. Nix, *Ionics* **2000**, *6*, 57–63.
[29] X. H. Liu, L. Zhong, S. Huang, S. X. Mao, T. Zhu, J. Y. Huang, *ACS Nano* **2012**, *6*, 1522–1531.
[30] M. H. Park, M. G. Kim, J. Joo, K. Kim, J. Kim, S. Ahn, Y. Cui, J. Cho, *Nano Lett.* **2009**, *9*, 3844–3847.
[31] R. Ruffo, S. S. Hong, C. K. Chan, R. A. Huggins, Y. Cui, *J. Phys. Chem. C* **2009**, *113*, 11390–11398.
[32] C. K. Chan, R. Ruffo, S. S. Hong, Y. Cui, *J. Power Sources* **2009**, *189*, 1132–1140.
[33] S. Misra, N. Liu, J. Nelson, S. S. Hong, Y. Cui, M. F. Toney, *ACS Nano* **2012**, *6*, 5465–5473.
[34] H. Wu, Y. Cui, *Nano Today* **2012**, *7*, 414–429.
[35] W.-J. Zhang, *J. Power Sources* **2011**, *196*, 877–885.
[36] G. Ji, Y. Ma, J. Y. Lee, *J. Mater. Chem.* **2011**, *21*, 9819–9824.
[37] K. Rhodes, N. Dudney, E. Lara-Curzio, C. Daniel, *J. Electrochem. Soc.* **2010**, *157*, A1354–A1360.
[38] M. J. Chon, V. A. Sethuraman, A. McCormick, V. Srinivasan, P. R. Guduru, *Phys. Rev. Lett.* **2011**, *107*.
[39] B. Key, M. Morcrette, J.-M. Tarascon, C. P. Grey, *J. Am. Chem. Soc.* **2010**, *133*, 503–512.
[40] H. Li, X. J. Huang, L. Q. Chen, G. W. Zhou, Z. Zhang, D. P. Yu, Y. J. Mo, N. Pei, *Solid State Ionics* **2000**, *135*, 181–191.
[41] X. H. Liu, J. W. Wang, S. Huang, F. Fan, X. Huang, Y. Liu, S. Krylyuk, J. Yoo, S. A. Dayeh, A. V. Davydov, S. X. Mao, S. T. Picraux, S. Zhang, J. Li, T. Zhu, J. Y. Huang, *Nat. Nanotechnol.* **2012**, *7*, 749–756.
[42] B. Key, R. Bhattacharyya, M. Morcrette, V. Seznec, J. M. Tarascon, C. P. Grey, *J. Am. Chem. Soc.* **2009**, *131*, 9239–9249.
[43] J. H. Ryu, J. W. Kim, Y.-E. Sung, S. M. Oh, *Electrochem. Solid-State Lett.* **2004**, *7*, A306–A309.
[44] C. v. d. Mare, G. J. B. Vinke, W. v. d. Lugt, *Solid State Commun.* **1985**, *54*, 917–919.
[45] H. Okamoto, *Bull. Alloy Phase Diagr.* **1990**, *11*, 306–312.
[46] V. L. Chevrier, J. R. Dahn, *J. Electrochem. Soc.* **2009**, *156*, A454–A458.
[47] J. Li, J. R. Dahn, *J. Electrochem. Soc.* **2007**, *154*, A156–A161.
[48] X. H. Liu, L. Q. Zhang, L. Zhong, Y. Liu, H. Zheng, J. W. Wang, J.-H. Cho, S. A. Dayeh, S. T. Picraux, J. P. Sullivan, S. X. Mao, Z. Z. Ye, J. Y. Huang, *Nano Lett.* **2011**, *11*, 2251–2258.
[49] C.-M. Wang, X. Li, Z. Wang, W. Xu, J. Liu, F. Gao, L. Kovarik, J.-G. Zhang, J. Howe, D. J. Burton, Z. Liu, X. Xiao, S. Thevuthasan, D. R. Baer, *Nano Lett.* **2012**, *12*, 1624–1632.
[50] M. T. McDowell, S. Woo Lee, C.-M. Wang, Y. Cui, *Nano Energy* **2012**, *1*, 401–410.
[51] M. T. McDowell, I. Ryu, S. W. Lee, C.-M. Wang, W. D. Nix, Y. Cui, *Adv. Mater. (Weinheim, Ger.)* **2012**, *24*, 6034–6041.
[52] H. Ghassemi, M. Au, N. Chen, P. A. Heiden, R. S. Yassar, *ACS Nano* **2011**, *5*, 7805–7811.
[53] K. Kang, H. S. Lee, D. W. Han, G. S. Kim, D. Lee, G. Lee, Y. M. Kang, M. H. Jo, *Appl. Phys. Lett.* **2010**, *96*, 3.
[54] J. Y. Kwon, J. H. Ryu, S. M. Oh, *Electrochim. Acta* **2010**, *55*, 8051–8055.
[55] V. L. Chevrier, J. W. Zwanziger, J. R. Dahn, *J. Alloys Compd.* **2010**, *496*, 25–36.
[56] S. W. Lee, M. T. McDowell, J. W. Choi, Y. Cui, *Nano Lett.* **2011**, *11*, 3034–3039.
[57] J. L. Goldman, B. R. Long, A. A. Gewirth, R. G. Nuzzo, *Adv. Funct. Mater.* **2011**, *21*, 2412–2422.
[58] X. H. Liu, H. Zheng, L. Zhong, S. Huan, K. Karki, L. Q. Zhang, Y. Liu, A. Kushima, W. T. Liang, J. W. Wang, J. H. Cho, E. Epstein, S. A. Dayeh, S. T. Picraux, T. Zhu, J. Li, J. P. Sullivan, J. Cumings, C. S. Wang, S. X. Mao, Z. Z. Ye, S. L. Zhang, J. Y. Huang, *Nano Lett.* **2011**, *11*, 3312–3318.
[59] S. W. Lee, L. A. Berla, M. T. McDowell, W. D. Nix, Y. Cui, *Isr. J. Chem.* **2012**, *52*, 1118–1123.
[60] R. N. Castellano, P. H. Schmidt, *J. Electrochem. Soc.* **1971**, *118*, 653.
[61] J. F. Nye, *Physical Properties of Crystals: Their Representation by Tensors and Matrices*, Oxford University Press, Oxford **1957**.
[62] K. J. Zhao, M. Pharr, Q. Wan, W. L. Wang, E. Kaxiras, J. J. Vlassak, Z. G. Suo, *J. Electrochem. Soc.* **2012**, *159*, A238–A243.
[63] H. Yang, S. Huang, X. Huang, F. Fan, W. Liang, X. H. Liu, L.-Q. Chen, J. Y. Huang, J. Li, T. Zhu, S. Zhang, *Nano Lett.* **2012**, *12*, 1953–1958.
[64] M. Pharr, K. Zhao, X. Wang, Z. Suo, J. J. Vlassak, *Nano Lett.* **2012**, *12*, 5039–5047.
[65] K. E. Bean, *IEEE Trans. Electron Dev.* **1978**, *25*, 1185–1193.
[66] M. K. Y. Chan, B. R. Long, A. A. Gewirth, J. P. Greeley, *J. Phys. Chem. Lett.* **2011**, *2*, 3092–3095.
[67] M. K. Y. Chan, C. Wolverton, J. P. Greeley, *J. Am. Chem. Soc.* **2012**, *134*, 14362–14374.
[68] L. Y. Beaulieu, T. D. Hatchard, A. Bonakdarpour, M. D. Fleischauer, J. R. Dahn, *J. Electrochem. Soc.* **2003**, *150*, A1457–A1464.
[69] V. L. Chevrier, J. R. Dahn, *J. Electrochem. Soc.* **2010**, *157*, A392–A398.
[70] J. Li, A. Smith, R. J. Sanderson, T. D. Hatchard, R. A. Dunlap, J. R. Dahn, *J. Electrochem. Soc.* **2009**, *156*, A283–A288.
[71] T. D. Hatchard, J. R. Dahn, *J. Electrochem. Soc.* **2004**, *151*, A838–A842.
[72] M. T. McDowell, S. W. Lee, J. T. Harris, B. A. Korgel, C.-M. Wang, W. D. Nix, Y. Cui, **2013**, *13*, 758–764.
[73] J. W. Wang, Y. He, F. Fan, X. H. Liu, S. Xia, Y. Liu, C. T. Harris, H. Li, J. Y. Huang, S. X. Mao, T. Zhu, *Nano Lett.* **2013**, *13*, 709–715.
[74] R. Deshpande, Y. T. Cheng, M. W. Verbrugge, *J. Power Sources* **2010**, *195*, 5081–5088.
[75] Y. T. Cheng, M. W. Verbrugge, *J. Electrochem. Soc.* **2010**, *157*, A508–A516.
[76] M. W. Verbrugge, Y. T. Cheng, *J. Electrochem. Soc.* **2009**, *156*, A927–A937.
[77] Y. T. Cheng, M. W. Verbrugge, *J. Power Sources* **2009**, *190*, 453–460.
[78] Y. T. Cheng, M. W. Verbrugge, *J. Appl. Phys.* **2008**, *104*, 083521.
[79] S. Golmon, K. Maute, S. H. Lee, M. L. Dunn, *Appl. Phys. Lett.* **2010**, *97*, 033111.
[80] C. M. DeLuca, K. Maute, M. L. Dunn, *J. Power Sources* **2011**, *196*, 9672–9681.
[81] I. Ryu, J. W. Choi, Y. Cui, W. D. Nix, *J. Mech. Phys. Solids* **2011**, *59*, 1717–1730.
[82] R. Grantab, V. B. Shenoy, *J. Electrochem. Soc.* **2012**, *159*, A584–A591.
[83] H. Haftbaradaran, H. J. Gao, W. A. Curtin, *Appl. Phys. Lett.* **2010**, *96*, 3.
[84] Y. F. Gao, M. Zhou, *J. Appl. Phys.* **2011**, *109*, 014310.
[85] H. Haftbaradaran, J. Song, W. A. Curtin, H. J. Gao, *J. Power Sources* **2011**, *196*, 361–370.
[86] V. A. Sethuraman, M. J. Chon, M. Shimshak, V. Srinivasan, P. R. Guduru, *J. Power Sources* **2010**, *195*, 5062–5066.
[87] K. J. Zhao, M. Pharr, S. Q. Cai, J. J. Vlassak, Z. G. Suo, *J. Am. Ceram. Soc.* **2011**, *94*, S226–S235.

Adv. Mater. **2013**,
DOI: 10.1002/adma.201301795

[88] K. J. Zhao, W. L. Wang, J. Gregoire, M. Pharr, Z. G. Suo, J. J. Vlassak, E. Kaxiras, *Nano Lett.* **2011**, *11*, 2962–2967.
[89] A. F. Bower, P. R. Guduru, V. A. Sethuraman, *J. Mech. Phys. Solids* **2011**, *59*, 804–828.
[90] K. J. Zhao, M. Pharr, J. J. Vlassak, Z. G. Suo, *J. Appl. Phys.* **2011**, *109*, 016110.
[91] Z. Cui, F. Gao, J. Qu, *J. Mech. Phys. Solids* **2012**, *60*, 1280–1295.
[92] F. Larché, J. W. Cahn, *Acta Metallurgica* **1973**, *21*, 1051–1063.
[93] R. Deshpande, Y.-T. Cheng, M. W. Verbrugge, A. Timmons, *J. Electrochem. Soc.* **2011**, *158*, A718–A724.
[94] S. W. Lee, M. T. McDowell, L. A. Berla, W. D. Nix, Y. Cui, *Proc. Natl. Acad. Sci. USA* **2012**, *109*, 4080–4085.
[95] W. H. Woodford, Y.-M. Chiang, W. C. Carter, *J. Electrochem. Soc.* **2010**, *157*, A1052–A1059.
[96] Y. Hu, X. Zhao, Z. G. Suo, *J. Mater. Res.* **2010**, *25*, 1007–1010.
[97] K. J. Zhao, M. Pharr, J. J. Vlassak, Z. G. Suo, *J. Appl. Phys.* **2010**, *108*, 073517.
[98] Y.-T. Cheng, M. W. Verbrugge, *Electrochem. Solid-State Lett.* **2010**, *13*, A128–A131.
[99] T. K. Bhandakkar, H. J. Gao, *Int. J. Solids Structures* **2011**, *48*, 2304–2309.
[100] T. K. Bhandakkar, H. J. Gao, *Int. J. Solids Structures* **2010**, *47*, 1424–1434.
[101] C. Y. Chou, H. Kim, G. S. Hwang, *J. Phys. Chem. C* **2011**, *115*, 20018–20026.
[102] H. Kim, C. Y. Chou, J. G. Ekerdt, G. S. Hwang, *J. Phys. Chem. C* **2011**, *115*, 2514–2521.
[103] V. B. Shenoy, P. Johari, Y. Qi, *J. Power Sources* **2010**, *195*, 6825–6830.
[104] V. L. Chevrier, J. W. Zwanziger, J. R. Dahn, *Can. J. Phys.* **2009**, *87*, 625–632.
[105] S. J. Lee, J. K. Lee, S. H. Chung, H. Y. Lee, S. M. Lee, H. K. Baik, *J. Power Sources* **2001**, *97-8*, 191–193.
[106] S. K. Soni, B. W. Sheldon, X. Xiao, A. Tokranov, *Scr. Mater.* **2011**, *64*, 307–310.
[107] S. K. Soni, B. W. Sheldon, X. Xiao, M. W. Verbrugge, D. Ahn, H. Haftbaradaran, H. Gao, *J. Electrochem. Soc.* **2012**, *159*, A38–A43.
[108] X. Xiao, P. Liu, M. W. Verbrugge, H. Haftbaradaran, H. Gao, *J. Power Sources* **2011**, *196*, 1409–1416.
[109] V. A. Sethuraman, V. Srinivasan, A. F. Bower, P. R. Guduru, *J. Electrochem. Soc.* **2010**, *157*, A1253–A1261.
[110] B. W. Sheldon, S. K. Soni, X. Xiao, Y. Qi, *Electrochem. Solid-State Lett.* **2012**, *15*, A9–A11.
[111] M. T. McDowell, S. W. Lee, I. Ryu, H. Wu, W. D. Nix, J. W. Choi, Y. Cui, *Nano Lett.* **2011**, *11*, 4018–4025.
[112] X. H. Liu, F. Fan, H. Yang, S. Zhang, J. Y. Huang, T. Zhu, *ACS Nano* **2012**, *7*, 1495-1503.
[113] J. C. Li, A. K. Dozier, Y. C. Li, F. Q. Yang, Y. T. Cheng, *J. Electrochem. Soc.* **2011**, *158*, A689–A694.
[114] J. P. Maranchi, A. F. Hepp, A. G. Evans, N. T. Nuhfer, P. N. Kumta, *J. Electrochem. Soc.* **2006**, *153*, A1246–A1253.
[115] T. Takamura, S. Ohara, M. Uehara, J. Suzuki, K. Sekine, *J. Power Sources* **2004**, *129*, 96–100.
[116] C. Yu, X. Li, T. Ma, J. Rong, R. Zhang, J. Shaffer, Y. An, Q. Liu, B. Wei, H. Jiang, *Adv. Energy Mater.* **2012**, *2*, 68–73.
[117] S. Kalnaus, K. Rhodes, C. Daniel, *J. Power Sources* **2011**, *196*, 8116–8124.
[118] V. A. Sethuraman, K. Kowolik, V. Srinivasan, *J. Power Sources* **2011**, *196*, 393–398.
[119] X. Li, P. Meduri, X. Chen, W. Qi, M. H. Engelhard, W. Xu, F. Ding, J. Xiao, W. Wang, C. Wang, J.-G. Zhang, J. Liu, *J. Mater. Chem.* **2012**, *22*, 11014–11017.
[120] K. J. Zhao, M. Pharr, L. Hartle, J. J. Vlassak, Z. G. Suo, *J. Power Sources* **2012**, *218*, 6–14.
[121] V. A. Sethuraman, M. J. Chon, M. Shimshak, N. Van Winkle, P. R. Guduru, *Electrochem. Commun.* **2010**, *12*, 1614–1617.
[122] J. B. Ratchford, B. A. Crawford, J. Wolfenstine, J. L. Allen, C. A. Lundgren, *J. Power Sources* **2012**, *211*, 1–3.
[123] J. B. Ratchford, B. E. Schuster, B. A. Crawford, C. A. Lundgren, J. L. Allen, J. Wolfenstine, *J. Power Sources* **2011**, *196*, 7747–7749.
[124] B. Hertzberg, J. Benson, G. Yushin, *Electrochem. Commun.* **2011**, *13*, 818–821.
[125] K. Zhao, G. A. Tritsaris, M. Pharr, W. L. Wang, O. Okeke, Z. Suo, J. J. Vlassak, E. Kaxiras, *Nano Lett.* **2012**, *12*, 4397–4403.
[126] S. T. Boles, A. Sedlmayr, O. Kraft, R. Monig, *Appl. Phys. Lett.* **2012**, *100*, 243901–243904.
[127] L. Hyunsoo, S. Weonho, C. Jang Wook, P. Jeong Young, *J. Phys. D: Appl. Phys.* **2012**, *45*, 275301.
[128] A. Kushima, J. Y. Huang, J. Li, *ACS Nano* **2012**, *6*, 9425–9432.
[129] W. Liang, H. Yang, F. Fan, Y. Liu, X. H. Liu, J. Y. Huang, T. Zhu, S. Zhang, *ACS Nano* **2013**, *7*, 3427–3433.
[130] X. H. Liu, Y. Liu, A. Kushima, S. Zhang, T. Zhu, J. Li, J. Y. Huang, *Adv. Energy Mater.* **2012**, *2*, 722–741.
[131] X. H. Liu, S. Huang, S. T. Picraux, J. Li, T. Zhu, J. Y. Huang, *Nano Lett.* **2011**, *11*, 3991–3997.
[132] J. W. Choi, J. McDonough, S. Jeong, J. S. Yoo, C. K. Chan, Y. Cui, *Nano Lett.* **2010**, *10*, 1409–1413.
[133] K. E. Aifantis, M. Haycock, P. Sanders, S. A. Hackney, *Mater. Sci. Engin. A* **2011**, *529*, 55–61.
[134] L. Xu, C. Kim, A. K. Shukla, A. Dong, T. M. Mattox, D. J. Milliron, J. Cabana, *Nano Lett.* **2013**, *13*, 1800–1805.
[135] L. Y. Beaulieu, S. D. Beattie, T. D. Hatchard, J. R. Dahn, *J. Electrochem. Soc.* **2003**, *150*, A419–A424.
[136] S.-C. Chao, Y.-F. Song, C.-C. Wang, H.-S. Sheu, H.-C. Wu, N.-L. Wu, *J. Phys. Chem. C* **2011**, *115*, 22040–22047.
[137] S.-C. Chao, Y.-C. Yen, Y.-F. Song, Y.-M. Chen, H.-C. Wu, N.-L. Wu, *Electrochem. Commun.* **2010**, *12*, 234–237.
[138] C.-F. Sun, K. Karki, Z. Jia, H. Liao, Y. Zhang, T. Li, Y. Qi, J. Cumings, G. W. Rubloff, Y. Wang, *ACS Nano* **2013**, *7*, 2717–2724.
[139] A. Kushima, X. H. Liu, G. Zhu, Z. L. Wang, J. Y. Huang, J. Li, *Nano Lett.* **2011**, *11*, 4535–4541.
[140] J. Y. Huang, L. Zhong, C. M. Wang, J. P. Sullivan, W. Xu, L. Q. Zhang, S. X. Mao, N. S. Hudak, X. H. Liu, A. Subramanian, H. Y. Fan, L. A. Qi, A. Kushima, J. Li, *Science* **2010**, *330*, 1515–1520.
[141] X. Wang, D.-M. Tang, H. Li, W. Yi, T. Zhai, Y. Bando, D. Golberg, *Chem. Commun. (Cambridge, U. K.)* **2012**, *48*, 4812–4814.
[142] C.-M. Wang, W. Xu, J. Liu, J.-G. Zhang, L. V. Saraf, B. W. Arey, D. Choi, Z.-G. Yang, J. Xiao, S. Thevuthasan, D. R. Baer, *Nano Lett.* **2011**, *11*, 1874–1880.
[143] L. Q. Zhang, X. H. Liu, Y. Liu, S. Huang, T. Zhu, L. J. Gui, S. X. Mao, Z. Z. Ye, C. M. Wang, J. P. Sullivan, J. Y. Huang, *ACS Nano* **2011**, *5*, 4800–4809.
[144] N. Balke, S. Jesse, A. N. Morozovska, E. Eliseev, D. W. Chung, Y. Kim, L. Adamczyk, R. E. Garcia, N. J. Dudney, S. V. Kalinin, *Nat. Nanotechnol.* **2010**, *5*, 749–754.
[145] N. Balke, S. Jesse, Y. Kim, L. Adamczyk, A. Tselev, I. N. Ivanov, N. J. Dudney, S. V. Kalinin, *Nano Lett.* **2010**, *10*, 3420–3425.

ADVANCED ENERGY MATERIALS

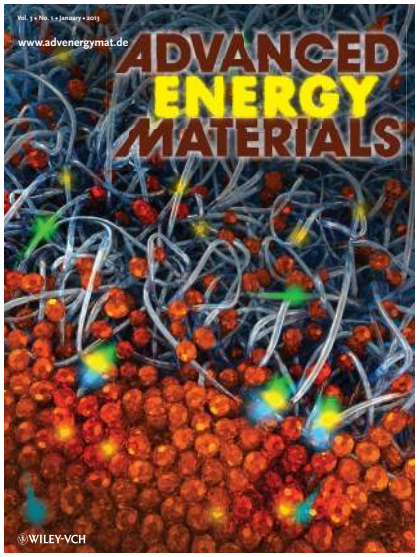

Cover picture by Harald Ade et al.

DOI: 10.1002/aenm.201200377

First Impact Factor

10.043

Advanced Energy Materials is an international, interdisciplinary, English-language journal of original peer-reviewed contributions on materials used in all forms of energy harvesting, conversion and storage.

Volume 3, 12 issues in 2013.
Print ISSN: 1614-6832.
Online ISSN: 1614-6840.

Highly Cited Papers on solar cells, batteries, supercapacitors, fuel cells, thermoelectrics:

Interdiffusion of PCBM and P3HT Reveals Miscibility in a Photovoltaically Active Blend
N. D. Treat, M. A. Brady, G. Smith, M. F. Toney, E. J. Kramer, C. J. Hawker, M. L. Chabinyc
http://onlinelibrary.wiley.com/doi/10.1002/aenm.201000023/full

All-Solid-State Lithium-Ion Microbatteries: A Review of Various Three-Dimensional Concepts
J. F. M. Oudenhoven, L. Baggetto, P. H. L. Notten
http://onlinelibrary.wiley.com/doi/10.1002/aenm.201000002/full

Graphene–Cellulose Paper Flexible Supercapacitors
*Zhe Weng, Yang Su, Da-Wei Wang, Feng Li, Jinhong Du, Hui-Ming Cheng**
http://onlinelibrary.wiley.com/doi/10.1002/aenm.201100312/full

Beyond 11% Efficiency: Characteristics of State-of-the-Art $Cu_2ZnSn(S,Se)_4$ Solar Cells
*T. K. Todorov, J. Tang, S. Bag, Oki Gunawan, Tayfun Gokmen, Yu Zhu, and David B. Mitzi**
http://onlinelibrary.wiley.com/doi/10.1002/aenm.201200348/full

Recent Progress in the Development of Anode Materials for Solid Oxide Fuel Cells
P. I. Cowin, C. T. G. Petit, R. Lan, J. T. S. Irvine, S. Tao
http://onlinelibrary.wiley.com/doi/10.1002/aenm.201100108/full

Thermoelectric Property Studies on Cu-Doped n-type $CuxBi_2Te_{2.7}Se_{0.3}$ Nanocomposites
W.-S. Liu, Q. Zhang, Y. Lan, S. Chen, X. Yan, Q. Zhang, H. Wang, D. Wang, G. Chen, Z. Ren
http://onlinelibrary.wiley.com/doi/10.1002/aenm.201100149/full

WILEY-VCH

www.advenergymat.de